

Spring 1-1-2018

Continuous Solar Observation from Low Earth Orbit with a Two-Cubesat Constellation

Jennifer Lauren Kampmeier

University of Colorado at Boulder, jennykampmeier@gmail.com

Follow this and additional works at: https://scholar.colorado.edu/asen_gradetds

 Part of the [Aerospace Engineering Commons](#), and the [Atmospheric Sciences Commons](#)

Recommended Citation

Kampmeier, Jennifer Lauren, "Continuous Solar Observation from Low Earth Orbit with a Two-Cubesat Constellation" (2018). *Aerospace Engineering Sciences Graduate Theses & Dissertations*. 204.
https://scholar.colorado.edu/asen_gradetds/204

This Thesis is brought to you for free and open access by Aerospace Engineering Sciences at CU Scholar. It has been accepted for inclusion in Aerospace Engineering Sciences Graduate Theses & Dissertations by an authorized administrator of CU Scholar. For more information, please contact cuscholaradmin@colorado.edu.

CONTINUOUS SOLAR OBSERVATION FROM LOW EARTH ORBIT
WITH A TWO-CUBESAT CONSTELLATION

by

JENNIFER LAUREN KAMPMEIER

A thesis submitted to the
Faculty of the Graduate School of the
University of Colorado in partial fulfillment
of the requirement for the degree of
Master of Science

Department of Aerospace Engineering Sciences

2018

This thesis entitled:
Continuous Solar Observation from Low Earth Orbit with a Two-CubeSat Constellation
written by Jennifer Lauren Kampmeier
has been approved for the Department of Aerospace Engineering Sciences

Robert A. Marshall, Committee Chair

Daniel Kubitschek, Committee Member

Date _____

The final copy of this thesis has been examined by the signatories, and we find that both the content and the form meet acceptable presentation standards of scholarly work in the above mentioned discipline.

Kampmeier, Jennifer Lauren (M.S., Aerospace Engineering Sciences)

Continuous Solar Observation from Low Earth Orbit with a Two-CubeSat Constellation

Thesis directed by Assistant Professor Dr. Robert A. Marshall

The goal of this work is to assess the feasibility of using a two-CubeSat constellation to make continuous solar science measurements from low Earth orbit. There is a growing interest in using CubeSats for scientific missions since they are relatively inexpensive, can be manufactured quickly, and they have a standard form factor. CubeSats have increased access to space, and there is a growing interest in the solar science community to be able to conduct remote sensing solar science missions from a CubeSat platform. By using a constellation separated by differential drag, this mission concept enables continuous measurements of the sun, allowing scientists to have a complete record despite the spacecraft's eclipse periods. In this thesis, I have developed a two-body propagator that takes various inputs for starting altitude, density model, attitude, and spacecraft configuration to enable investigation over a large trade space. Following the model development, I ran a series of simulations to explore the feasibility of this concept, finding that there are many combinations of parameters that produce a feasible mission design. I show that the model is validated by altitude decay data from the MinXSS CubeSat, I will discuss areas of the design that require further study, and I explore the logical next steps for future development of this concept.

Dedication

This work is dedicated to my husband Matt Muszynski, who jumped off the cliff with me and helped me build my wings on the way down. There is no one I would rather have by my side, and I quite literally could not have done this without you.

—JK

Acknowledgements

I would like to thank my advisor, Dr. Robert Marshall for his tireless support, mentorship, and confidence in me during my last two years of school at CU Boulder. I am grateful that our paths have crossed at this university, and I hope to repeat that good fortune again in the future. I would also like to thank Dr. Scott Palo and Dr. Dan Kubitschek for their willingness to serve on my committee despite having longer to-do lists than most people I know. Finally, I would like to thank my family and my friends for putting up with me for the last five years—while I sacrificed a lot for this degree, they graciously allowed me to stay in their lives despite my perpetual lack of sleep and too-infrequent phone calls.

Contents

1	Introduction	1
1.1	Differential Drag	2
1.2	International Space Station Orbit	3
1.3	Sun-Synchronous Dawn/Dusk Polar Orbit	4
1.4	Time Scales of Solar Phenomena	5
2	Background	8
2.1	CubeSat Constellations	9
2.1.1	AeroCube 6	10
2.1.2	Planet Labs CubeSat Constellation	11
2.2	Other Spacecraft Constellations	13
2.3	Instruments for Solar Science	15
3	Methodology	16
3.1	Assumptions and Basic Information	16
3.1.1	ISS Orbit	16
3.1.2	Concept of Operations	18
3.1.3	Cross-Sectional Areas and Notional Spacecraft Designs	19
3.1.4	Body Frame Coordinate Axis Definition	22
3.1.5	Selection of Solar Minimum and Solar Maximum Conditions	22
3.2	Two-Body Propagator	24
3.3	Propagation with ode45	26
3.3.1	Density Model—Exponential	27
3.3.2	Density Model—Naval Research Laboratory’s MSISE-00 Model	28
3.4	Adding the Drag Force	32
4	Results and Discussion	38
4.1	Baseline Simulation	39
4.2	Mission Duration and Length of Commissioning Phase	42
4.3	Comparing the Two Density Models	45
4.4	Comparison with MinXSS altitude data	47
4.5	Adding Additional CubeSats to the Constellation	48
4.6	Asynchronous CubeSat Deployments	49
4.7	Results Summary	50
5	Applications and Future Work	51
5.1	Adding a Control Algorithm	51
5.2	Thermospheric Winds	52
5.3	Science Impact of the Commissioning Phase	53
5.4	The Effect of Atomic Oxygen	54
5.5	A More Comprehensive Gravity Model	56
5.6	Self-Shadowing of Spacecraft Body by Solar Panels	57
6	Summary	59

References	60
Appendix	66

List of Tables

1	Representative orbital elements for the International Space Station orbit. . .	17
2	Notional spacecraft configurations.	20
3	$f_{10.7}$ and A_p values for solar maximum and minimum.	23
4	Algorithm 1.	25
5	Algorithm 2.	26
6	Algorithm 3	30
7	Inverse ballistic coefficients for each spacecraft configuration.	36
8	Data from baseline simulation for all spacecraft configurations.	40
9	Summary of space-based missions for remote sensing measurements of the Sun	66

List of Figures

1	X-ray flux from GOES 12 during the solar storms of October 2003.	5
2	Prototypes and flight models of the MinXSS CubeSat.	8
3	One of two 0.5U CubeSats that comprise the AeroCube 6 project.	11
4	On-orbit data of Planet Labs' Flock 1-C CubeSat constellation.	12
5	An artist's representation of the MMS constellation.	14
6	The Amptek spectrometer used on MinXSS.	15
7	Altitude of the ISS since launch.	17
8	Concept of operations.	19
9	Distribution of notional CubeSat configurations.	21
10	Spacecraft coordinate axes definition as shown on a sample CubeSat.	22
11	History of $f_{10.7}$ cm radio flux.	23
12	Change in cross-sectional area over a single orbit.	34
13	An example of self-shadowing.	35
14	Baseline simulation for all spacecraft configurations.	40
15	Slope change of altitude decay after maneuver.	41
16	Angular separation of the leader and follower for a full mission duration.	42
17	Length of commissioning vs. length of prime mission.	43
18	Length of commissioning vs. length of prime mission, zoomed in to show solar maximum conditions more clearly.	44
19	A direct comparison of the two density models.	45
20	An isolated data set to show the difference in density model.	46
21	Comparison of MinXSS altitude decay with simulation data.	48
22	Estimating eclipse duration based on orbital altitude.	51
23	Particle density composition of the atmosphere from 200 to 500 km during mean solar conditions.	54
24	Variation of C_D with altitude when accounting for the effects of atomic oxygen.	55
25	Comparing simulations with constant or variable C_D	56
26	Estimating the effect of self-shadowing.	58

Nomenclature

δ	Declination angle
λ	Longitude
μ_{\oplus}	Gravitational parameter for Earth
ν	True anomaly of an orbit
Ω	Right ascension of the ascending node (RAAN) of an orbit
ω	Argument of perigee of an orbit
ω_{\oplus}	Magnitude of the angular rotational velocity vector for the Earth
ϕ_{gd}	Geodetic Latitude
ρ	Atmospheric density
θ_{GMST}	Greenwich Mean Sidereal Time
A	Cross-sectional area of the spacecraft
a	Semi-major axis of an orbit
A_p	Geomagnetic index
C_D	Coefficient of drag of the spacecraft
e	Eccentricity of an orbit
e_{\oplus}	Eccentricity of the Earth
$f_{10.7}$	Solar radio flux at 10.7 cm
H	Scale height
h	Altitude of a spacecraft above the surface of the Earth
i	Inclination of an orbit
m	Mass of the spacecraft
m_{mol}	Molecular mass
P	Period of an orbit
p	Semiparameter of an orbit
r	Magnitude of the position vector in an Earth-centered inertial frame
r_{δ}	Equatorial projection of the satellite's IJK (ECEF) position vector

R_{\oplus} Radius of the Earth

T_{exo} Exospheric temperature

v Magnitude of the velocity vector of the spacecraft

v_{rel} Magnitude of the velocity vector of the spacecraft relative to the atmospheric rotation

1 Introduction

The first recorded solar observations date back to the Iron Age, when ancient Syrians and Babylonians regularly documented solar eclipses and were thought to be able to understand the phenomenon well enough to predict the next occurrence [1]. Since then, the cadence of recorded solar observation has consistently increased; since the space age began, many space missions have been launched for the express purpose of studying the Sun. The National Aeronautics and Space Administration (NASA) maintains a Heliophysics Division, which aims “to understand the Sun and its interactions with the Earth and the solar system, including space weather” [2]. Through this division, NASA allocates part of its budget every year to support programs that will further our understanding of the Sun, specifically soliciting proposals for cutting-edge scientific and technological advancements. With this in mind, I sought to explore a low-cost mission design idea that would introduce a new approach to conducting solar science.

Every year, NASA’s Low Cost Access to Space (LCAS) program supports novel techniques that encourage discoveries in heliophysics science through sounding rockets, CubeSat platforms, research balloons, and others [3]. The LCAS program is of particular interest for this project, since using CubeSats for solar science is a relatively recent and unexplored capability. CubeSats are small, self-sufficient spacecraft with standardized sizing, where each unit (“U”) is a 10 cm cube, arranged in pre-determined orientations such as 3U, which results in a 10 cm × 10 cm × 30 cm structure. CubeSats can range in size anywhere from 0.5U to 27U assemblies, and standardized dispensers exist such that CubeSats can be brought as “ride-along” payloads on larger missions. In particular, the regular resupply missions to the

International Space Station (ISS) often bring CubeSats as secondary payloads, so launching from the ISS has become a common practice for low Earth orbit (LEO) CubeSat missions.

One challenge with solar science is that continuous observation is desirable or even necessary—solar phenomena can happen on the order of minutes to days, so having gaps in the data makes it more difficult to study solar events in their entirety. However, this presents a problem for a CubeSat mission, since most will not have control over their exact orbit due to their nature as secondary payloads. Most CubeSats are launched into orbits where they will have eclipse periods, so regardless of the exact orbit, a percentage of their data collection time will be lost due to eclipse. This problem could be solved with a polar, dawn-dusk sun-synchronous orbit, but those launch opportunities are less frequent, and therefore the feasibility of launching into one of these orbits is decreased. Additionally, a dawn-dusk sun-synchronous orbit is challenging from a thermal perspective, as the constant solar heating can degrade spacecraft components more quickly. These constraints on CubeSat missions suggests a possible solution: what if we launched two identical CubeSats but spaced them apart in their orbit, such that eclipses are not impactful on the science outcome? More importantly, would this be a feasible and realistic mission concept? Before diving into this topic, some preliminary studies are necessary to determine whether this concept is feasible. The following sections outline this work and introduce some of the basics of this project.

1.1 Differential Drag

The concept of differential drag between two CubeSats is fairly simple—one spacecraft is designated as the “leader” and it maintains a low-drag attitude while the other

spacecraft (the “follower”) is maneuvered into a high-drag configuration in order to lower its orbit and therefore increase the distance between the two spacecraft until the desired separation is reached. As the follower’s orbit degrades it will have an increased velocity relative to the leader, and so at times this nomenclature may be confusing. Regardless, the “leader” spacecraft is always the one that began the initial separation in a low-drag configuration, and the “follower” spacecraft always begins with a high-drag configuration. As discussed later in Section 2, differential drag is not a new concept and many spacecraft constellations have successfully used differential drag to maintain a formation. What makes this case interesting is that there is such a large trade space to consider, and that the two spacecraft do not have to maintain an exact 180° separation in order to fulfill the goal of continuous (or nearly continuous) solar science collection.

1.2 International Space Station Orbit

From November 2017 to November 2018, there are 48 scheduled CubeSat missions that are part of NASA’s Educational Launch of Nanosatellites program (ELaNa), deploying from the International Space Station (ISS) [4]. While other launch opportunities and orbits are certainly possible, using the ISS orbit allows the problem to be constrained while keeping it practical for future launch opportunities. Since there have been many successful scientific CubeSats deployed from the ISS, using a proven orbit increases the feasibility of the overall mission.

While using an ISS orbit helps to constrain the problem, it also presents challenges.

Lower altitude orbits such as the ISS orbit at 400 km will shorten the mission duration,

depending on the design of the spacecraft, the attitude configuration, and solar conditions. For this concept to be feasible, the time it takes to separate the two spacecraft must not be so long that it significantly reduces the amount of science collection time available. It is clear that there will be a trade-off between mission duration, altitude, and the time it takes to separate the two spacecraft to $\sim 180^\circ$ orbit separation.

1.3 Sun-Synchronous Dawn/Dusk Polar Orbit

If I didn't constrain this project to an ISS orbit, there is a relatively simple orbital solution that would eliminate the necessity for a constellation of CubeSats. A sun-synchronous dawn/dusk polar orbit has a high inclination of approximately 98° , and a right ascension of the ascending node that allows the spacecraft to orbit along the terminator. This particular inclination allows the orbital precession rate to match Earth's speed as it travels around the Sun, hence the designation "sun-synchronous" [5]. This type of orbit would allow a spacecraft to stay in the sun at all times, enabling continuous solar observation with a single spacecraft platform. However, these orbits require more energy to launch into since they are slightly retrograde, and there are fewer CubeSat launch opportunities for this type of orbit. Additionally, spacecraft in these orbits can often have thermal issues since they are constantly in sunlight—components have a tendency to degrade under extreme thermal conditions, and so eclipses can be desirable to help keep the spacecraft within its thermal requirements. Lastly, one of the goals of this project is to explore a mission concept that increases access to space, so I chose to baseline the ISS orbit due to its large availability of deployment opportunities.

1.4 Time Scales of Solar Phenomena

Solar phenomena have a wide range of relevant time scales—events can happen on the order of seconds to days, and depending on the science investigation different time scales may be of interest. For example, the X-ray flux from solar flare events can spike in a few minutes and then decay over the course of several hours to days [6]. Fig. 1 shows the hard and soft X-ray flux as measured by the GOES 12 satellite on October 28, 2003 during a large solar storm event.

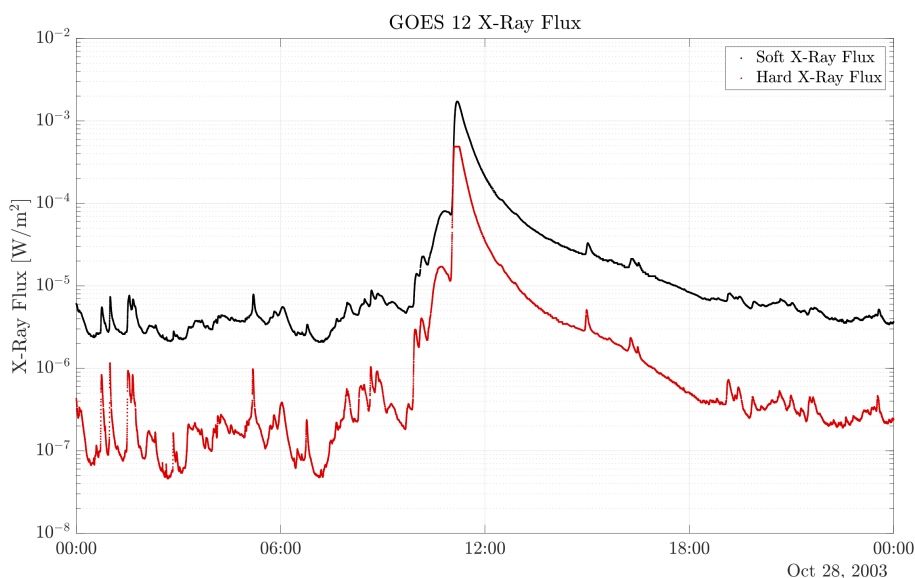


Figure 1: Soft and hard X-ray flux from GOES 12 during the solar storm of late October 2003. The large spike in flux is a powerful X-class solar flare, which develops from the nominal values to its largest peak in approximately 75 minutes. The jump in strength from an M-class to X-class flare occurs in approximately 11 minutes. Data is courtesy of the GOES Space Environment Monitor Data Access archive [6].

Before the flare, the hard X-ray flux (red curve) is stable with values ranging from 4.61×10^{-8} to 1.16×10^{-6} W/m², but at approximately 28-Oct-2003 at 09:51:28 UTC, the flux suddenly spikes over the course of approximately 75 minutes to strong X-class flare levels, and the transition from M-class to X-class occurs in only 11 minutes.

Coronal mass ejections (CMEs) can occur as often as six times per day during solar maximum and can arrive at Earth on average within 2 to 4 days, traveling at speeds that vary from <20 km/s to >3000 km/s with an average of approximately 470 km/s [7]. Fast-moving CMEs also have the ability to accelerate solar wind particles ahead of the CME, which can induce solar energetic particle (SEP) events. SEPs move very quickly, and can arrive at Earth on the order of minutes to hours. In general, SEP events have a range of characteristics and can last on the order of hours or days [7].

Flares, CMEs, and SEP events are just a few examples of solar phenomena that scientists may be interested in studying from a CubeSat platform—the MinXSS spacecraft has already begun the trend by studying soft X-ray distribution, and MinXSS-2 will continue studying these emissions during its mission [8]. Since this proposed mission concept will use a similar orbit to the ISS, we can expect eclipses to last approximately 35 minutes, which would be long enough to completely miss the eruption of a solar flare event. By using two identical, antipodal CubeSats, these phenomena could be captured despite eclipse periods.

To summarize, the purpose of this thesis is to assess the feasibility of using two CubeSats to provide continuous temporal observation of solar phenomena from low Earth orbit. Since most flight opportunities for CubeSats will place them into orbits with eclipses, continuous solar observation is not typically possible. But by using two identical CubeSats spaced approximately 180° apart in their orbits, it will be possible to maintain continuous science collection with a constellation rather than a single satellite. Additionally, deployment opportunities from the ISS are relatively common, so I will use an approximate ISS orbit

as a baseline, though I will also investigate altitudes up to 500 km. Additionally, a set of discrete spacecraft configurations and attitude schemes will be used for analysis, since this helps to constrain the problem while keeping the trade space manageable.

2 Background

In 2016, the MinXSS mission was launched with instruments to measure the solar soft X-ray spectrum, and in doing so it became the first solar science oriented CubeSat that was launched for the NASA Science Mission Directorate [10]. There have been a large number of CubeSat missions launched to make in-situ measurements of Earth's upper atmosphere, its magnetic field, space



Figure 2: Iterations of the MinXSS CubeSat from left to right: a prototype model used for early testing, Flight Model 1 which deployed from the ISS in 2016, and Flight Model 2 that will launch in 2018 [9].

weather, the Van Allen radiation belts, and other phenomena that occur from Earth-Sun interactions [11, 12, 13], but MinXSS was the first NASA CubeSat to have instruments explicitly designed to point at the Sun and take measurements of incoming photons [8]. Of course, there have been numerous full-scale space missions that study the Sun through remote sensing, such as the Solar Dynamics Observatory (SDO), the Solar and Heliospheric Observatory (SOHO), the Solar TERrestrial RELations Observatory (STEREO), the Solar Radiation and Climate Explorer (SORCE), plus instruments like the Total Spectral and Solar Irradiance Sensor (TSIS), which is currently onboard the ISS. The contributions that these missions have had to our understanding of the Sun cannot be overstated, and they form the foundation for the vast majority of our knowledge of how the Sun works.

The challenge with full-scale space missions is that they are costly, time-intensive to produce and operate, and there are more scientific investigation ideas than there are

mission opportunities. CubeSats present a solution to many of these challenges, since they are inexpensive, can be produced at a rapid cadence, and launch opportunities are common enough that more organizations, universities, and other entities can gain access to space. Of course, CubeSats come with their own difficulties since all components must be miniaturized, and often their capabilities are more limited because of their size. The mission length for a CubeSat tends to be shorter as well—they typically must plan to accomplish all of their scientific goals within a few months after launch to ensure success. However, because they provide a low barrier to entry, they are becoming a more popular platform to conduct space science, and CubeSats are beginning to make significant contributions to different fields in space science. Recently, a student-built CubeSat called the Colorado Student Space Weather Experiment (CSSWE) had its findings published in *Nature*, which solved a 60-year mystery about the origins of certain energetic particles in Earth’s radiation belts [14]. Clearly, CubeSats can be significantly impactful and make worthwhile scientific contributions.

2.1 CubeSat Constellations

Using CubeSat constellations to improve the scientific output of a single CubeSat mission is a relatively new idea, but it has been implemented successfully in a few cases. In 2014, the Canadian Advanced Nanospace eXperiment-4&5 (CanX-4 and CanX-5, or CanX-4&5) were launched specifically to demonstrate the ability of two 20 cm cube nanosatellites to fly in formation with tracking errors of less than 1 m, while requiring low fuel consumption to maintain the formation [15]. While this mission was a technology demonstration rather than a scientific investigation, it showed that coordinating two CubeSats to work together

is feasible, particularly if accurate spacecraft separation is required. Similarly, in a 2016 paper by Nag et al. entitled “CubeSat constellation design for air traffic monitoring”, the authors present detailed design options for several CubeSat constellations that could be used to provide real-time monitoring of aircraft [16]. Again, the purpose of their constellation designs is not to facilitate science, but their detailed analysis shows that large networks of CubeSats are feasible as a means of extending what is possible with a single spacecraft.

Another proposed constellation is the Temporal Experiment for Storms and Tropical Systems (TEMPEST) mission, a student-led CubeSat project at Colorado State University. TEMPEST is launching its first 6U demonstration satellite (TEMPEST-D) in May 2018, with the intent of launching a 5-satellite constellation in the future once certain components have been space-proven. TEMPEST is also interested in temporal measurements, albeit of the Earth rather than the Sun, and plans to use differential drag to separate the spacecraft in their orbit by 5-10 minutes each [17]. The Dynamic Ionosphere CubeSat Experiment (DICE) mission launched two identical 1.5U CubeSats in 2011 to take in-situ measurements of the ionosphere, although these two satellites were allowed to drift naturally based on the small difference in ejection speed from the deployer rather than use any sort of controlled orbit-keeping through differential drag or propulsion. DICE used the two satellites to resolve spatial and temporal ambiguities in their ionospheric measurements similar to other constellation missions [18].

2.1.1 AeroCube 6

AeroCube 6 was a project of The Aerospace Corporation, consisting of a pair of 0.5U CubeSats that were launched in 2015 with a dosimeter payload for measuring spatial

scales of radiation in low Earth orbit [19]. The CubeSats were deployed into the same orbit and successfully used differential drag to change their in-track relative position.

Both satellites used magnetic torque rods to control their attitude, so their attitude control was less precise than missions that use reaction wheels. During the mission, the two CubeSats successfully separated their in-track position by 800 km over approximately 10 weeks, and then closed the separation to 300 km after another 6 months on orbit (including a 1-month period where the differential drag was uncontrolled) [19].

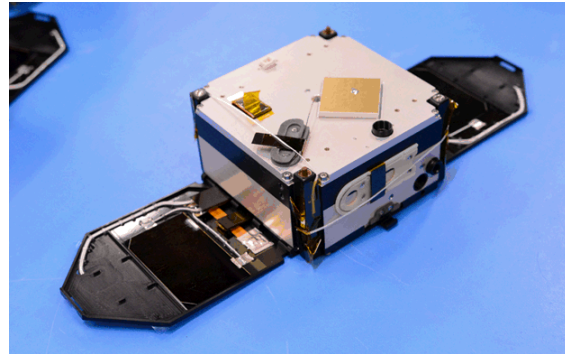


Figure 3: One of two 0.5U CubeSats that comprise the AeroCube 6 project from The Aerospace Corporation. After deployment, this two-CubeSat constellation used differential drag to control the relative in-track orbital position. The largest separation between the two CubeSats was approximately 800 km [19].

This mission showed that differential drag can be used to control the in-track position of CubeSats, and that this technique can be particularly useful for missions with interest in spatial scales of in-situ phenomena.

2.1.2 Planet Labs CubeSat Constellation

Planet Labs is a commercial space company whose goal is to launch and maintain large constellations of spacecraft to provide daily imaging of the entire planet. Planet Labs has accomplished this task with a fleet of 3U CubeSats, using differential drag to equally separate 100+ satellites in a single orbital plane. Previously, they have proven their ability to do this with a fleet of 10 3U CubeSats in 2014/2015 (shown in Fig. 4), again with a fleet of 12 CubeSats a year later [20], and today Planet Labs operates over 100 CubeSats whose

orbits are initialized and maintained using differential drag. In one instance, Planet Labs launched 88 CubeSats on a single launch vehicle into a ~ 500 km sun-synchronous orbit, and used a series of differential drag maneuvers to separate the spacecraft by 3 to 4° in the same orbital plane [21]. Each of their CubeSats contains a sophisticated control algorithm to determine when they should maneuver into a high-drag attitude configuration in order to keep a zero relative velocity between each spacecraft. They also use an independent orbit determination algorithm to accurately locate each CubeSat, since errors in publicly available two-line elements (TLEs) from the Joint Space Operations Center can exceed acceptable limits, particularly for spacecraft in low-altitude orbits where atmospheric drag significantly influences the orbit [20].

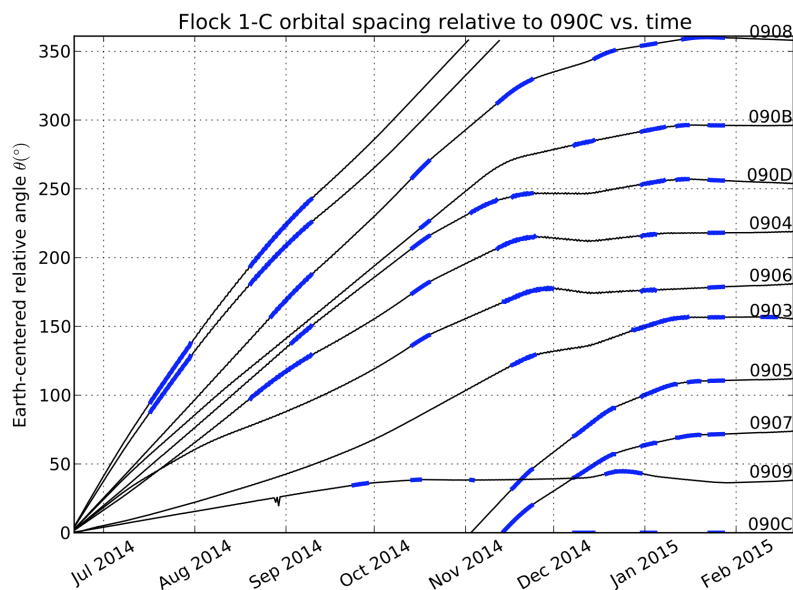


Figure 4: Figure from Foster et al. showing actual on-orbit data of Planet Labs' Flock 1-C CubeSat constellation. All 10 CubeSats start at approximately the same position following a consecutive deployment, and the thick blue lines indicate when each satellite was in its high-drag configuration. The final state of each spacecraft is shown with the desired in-track spacing and a zero relative mean motion achieved with only differential drag [20].

Clearly, Planet Labs has accomplished a significant goal in using differential drag to

maintain their fleet of 3U CubeSats. In this thesis, by employing many of the same strategies such as low-drag and high-drag configurations, and using differential drag to separate the constellation, I explore the feasibility of this type of mission under different constraints. The proposed mission concept is constrained to deploy from an ISS orbit, which will be a lower altitude than Planet Labs' constellations, and is not sun-synchronous. Similarly, an ideal orbit-in-the-life for this mission would have the instrument boresight pointed at the Sun when the spacecraft is in daylight, and to downlink in shadow, which will change the drag profile throughout the orbit. Another difference is that there is a greater acceptable in-track orbital error with my mission, since a true 180° separation is not required to maintain continuous solar science collection. The methodology and success of Planet Labs' constellations has certainly informed and influenced my research, and where appropriate I have given credit to their methods.

2.2 Other Spacecraft Constellations

Even though each type of constellation has unique challenges, the success of CubeSat constellations has been built on the foundation of full-scale spacecraft constellations. For example, the Cyclone Global Navigation Satellite System (CYGNSS) constellation consists of 8 identical spacecraft with a mission of monitoring inner-core wind speeds of tropical cyclones. The CYGNSS constellation is designed to be spread around the Earth in approximately the same orbital plane for full coverage, rather than flying close together to provide spatial or temporal measurements of in-situ phenomena [22].

In contrast, the Cluster, Swarm, and Magnetospheric Multiscale (MMS) constellations of satellites have been successfully operated with the goal of characterizing different aspects of Earth's magnetic fields. Cluster studies small-scale plasma

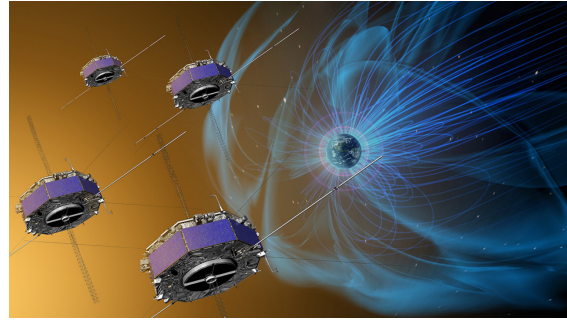


Figure 5: MMS is a constellation of four satellites studying magnetic reconnection at a range of time scales [23].

structures and plasma processes, Swarm studies the temporal evolution of Earth's magnetic fields, and MMS studies magnetic reconnection at a range of time scales [24, 25, 26]. The A-Train is a unique type of spacecraft constellation: it consists of five unique satellites from different space agencies, launched into the same orbit so that each satellite passes through the same portion of the orbit seconds-to-minutes apart. Each mission has a different science goal, from water and energy-cycle measurements to characterizing aerosols with lidar [27, 28]. This group of satellites has demonstrated the power of using formation flight and constellations:

As scientists and engineers refined their mission plans, they began to fully appreciate the potential advantages of formation flying. A single platform could not accommodate the mass and power demands of all the missions' instruments. Moreover, if they were all crowded together on a single craft, the sensors would get in each others' way and interfere electronically. Carefully coordinating the orbits of five individual satellites, however, would enable researchers to benefit from a unique multisensor perspective of our planet. [27]

These missions and others are building the foundation for the next generation of spacecraft constellations—by showing us that it is possible and beneficial, it allows more organizations, universities, and research labs to consider using spacecraft constellations to achieve their science goals.

2.3 Instruments for Solar Science

In general, solar science CubeSat missions will be interested in the same type of science as large-scale spacecraft, but their instruments tend to be smaller and more specialized. For example, rather than studying the entire spectra of X-ray emissions from the Sun, MinXSS used a miniaturized spectrometer from Amptek that focused on

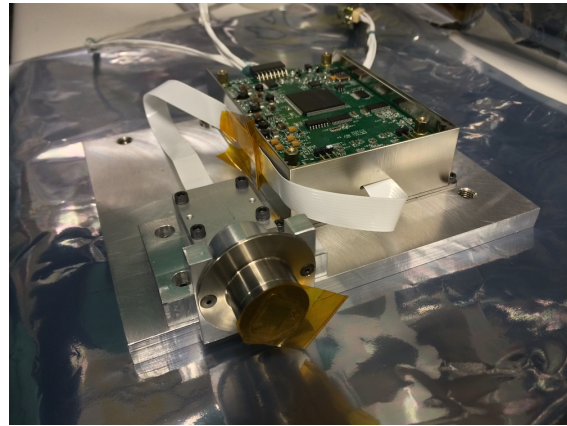


Figure 6: The Amptek spectrometer used on MinXSS, shown mounted to a plate for testing aboard a sounding rocket [29].

a small bandpass at a moderate level of resolution [8]. This allowed MinXSS to study a small but important region of solar emissions that had not been studied previously, enabling significant contributions to our knowledge of X-ray emissions from the Sun.

As shown in Table 9 in the Appendix, the instruments on flagship solar science missions have consisted of spectrometers, telescopes, and imagers, all designed for a specific scientific investigation. Since I am not constraining the specific instrument for this mission, preference is given to spacecraft configurations that allow larger depths for the boresight, since some instruments may require a collimator or long telescope housing that would benefit from a longer depth. In other words, if the instrument is allotted 2U or 3U of depth, that would be more valuable than a spacecraft configuration that only allots 1U of space for the instrument.

3 Methodology

As stated previously, the purpose of this thesis is to explore a mission design concept: to assess the feasibility of using two CubeSats to provide continuous temporal observation of solar phenomena from low Earth orbit. In this section, I will discuss the assumptions, algorithms, and methodology used to accomplish this goal. Through careful consideration of the variables involved in this project, I have assembled feasible mission scenarios for this mission concept.

3.1 Assumptions and Basic Information

3.1.1 ISS Orbit

Using the orbit of the International Space Station gives me a baseline to work from—the particular parameters of the ISS orbit change every day, and so the information presented in Table 1 is representative of one possible set of parameters. By far the most influential orbital element for this analysis is the semi-major axis, since larger orbital altitudes will allow spacecraft to decay more slowly than those that start at lower altitudes. An analysis of how this affects the results is included in later sections. Note that the true anomaly, ν , was arbitrarily chosen to be 0° for the starting point of the analysis, and that orbital elements were obtained from NORAD two-line element sets (TLEs) [30]. The altitude of the ISS changes rapidly because of drag, and since launch the altitude has varied between approximately 320 km and 420 km as shown in Figure 7. Recently the altitude has stayed around 405 km, and while this is a good baseline to consider, I have also considered altitudes up to 500 km since the Cygnus cargo resupply vehicle also offers the option of CubeSat

deployment at 500 km after Cygnus has completed its primary mission to the ISS [31].

Table 1: Representative orbital elements for the International Space Station orbit. Since these change slightly every day, analysis will be presented to show how changes in semi-major axis affect the results. Data in this table was obtained from two-line element sets from NORAD/CelesTrak [30].

Parameter	Value
Gravitational Parameter, μ_{\oplus}	$3.986004415 \times 10^5 \text{ km}^3/\text{s}^2$
Earth radius, R_{\oplus}	6,378.1363 km
Eccentricity, e	0.0003103
Inclination, i	51.6370°
RAAN, Ω	247.8226°
Argument of Perigee, ω	215.7581°
Semi-major axis, a	6,833.26 km
True anomaly, ν	0°
Period, P	5,621.50 s

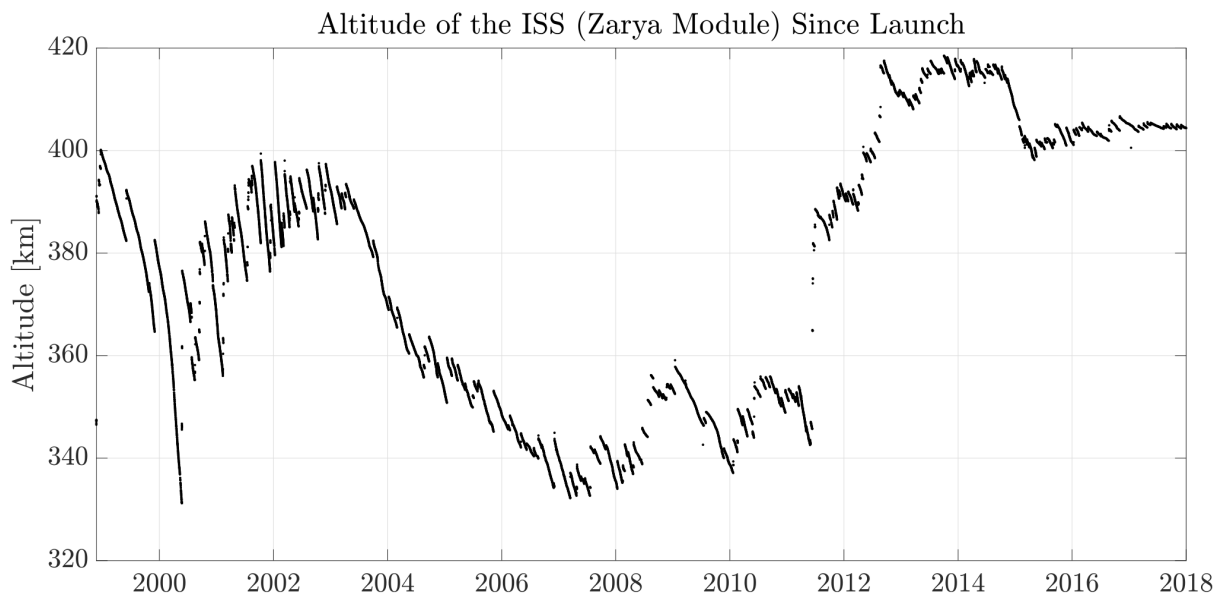


Figure 7: Altitude of the ISS since launch; recent altitudes are centered around 405 km [30].

3.1.2 Concept of Operations

As with many parts of this project, the concept of operations is notional and there are valid concepts that could be employed to similar effect. For the remainder of this analysis, the concept of operations under consideration consists of the following two phases:

1. Phase 1 (Commissioning): One spacecraft is in its high-drag configuration, and one spacecraft is in its low-drag configuration. This means that both spacecraft will have its high or low-drag profile pointed in the ram direction at all times, see Fig. 8. This ensures that the time needed to separate to 180° is minimized.
2. Phase 2 (Prime Mission): Both spacecraft will maneuver to be solar-pointed at all times, see Fig. 8. Keeping both spacecraft solar-pointed will allow for the maximum science operation time assuming nominal operations.

Although not included in the analysis, another possible configuration that may increase the amount of science data collected could only move into the differential drag configurations during eclipse periods, and stay solar-pointed in sunlight. This would extend the time needed to separate the spacecraft, but would allow science collection to start sooner. An underlying assumption in this analysis is that a shorter commissioning phase is desirable, but one could also imagine a scenario where Phase 1 is lengthened in order to decrease the amount of initial orbital decay, thereby increasing the amount of time spent in Phase 2. This is an operations concept that could be explored in future work on this topic.

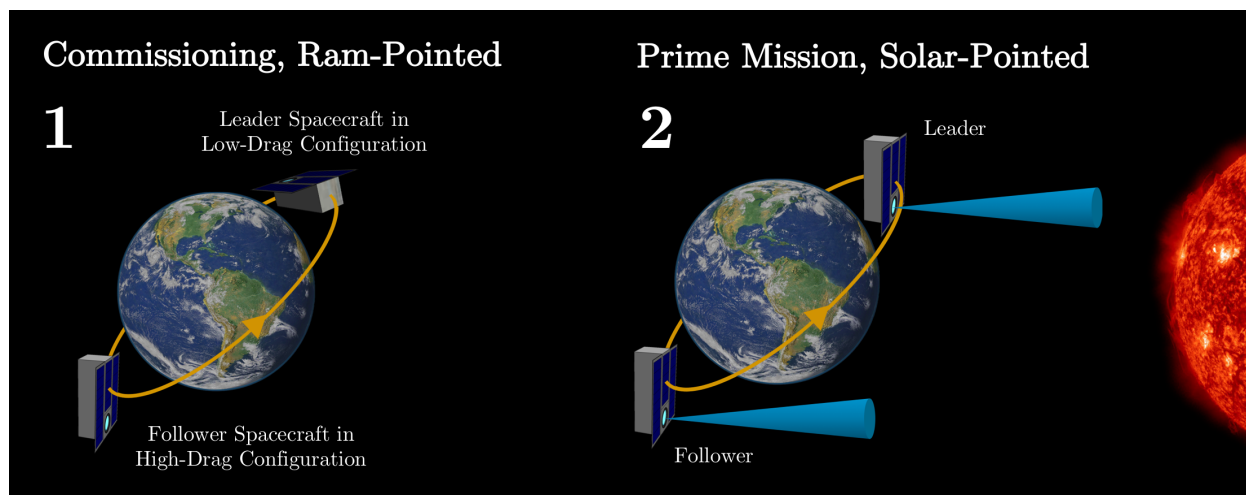


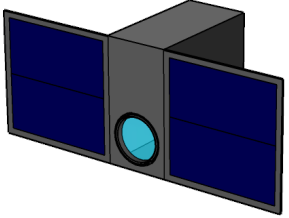
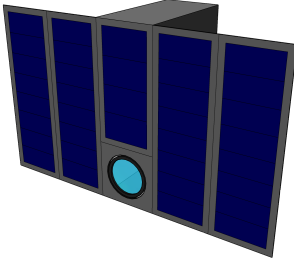
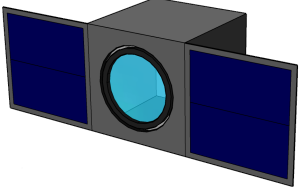
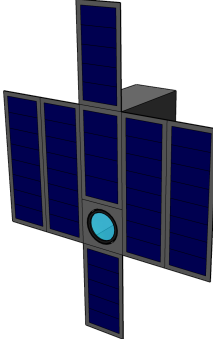
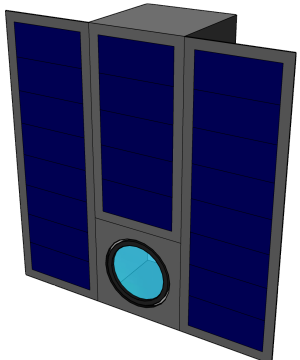
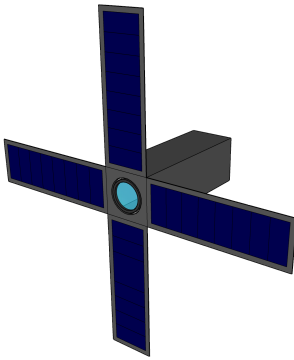
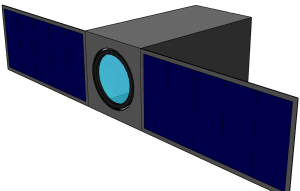
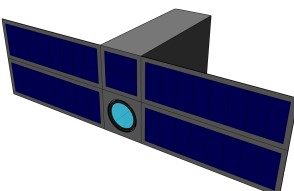
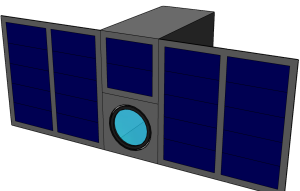
Figure 8: Phase 1 (Commissioning) of the concept of operations has one spacecraft in its high-drag configuration, and the other in a low-drag configuration, allowing the spacecraft to drift apart. Both spacecraft have their low- or high-drag profiles ram-pointed at all times. During Phase 2 (Prime Mission), both spacecraft are solar-pointed at all times during the orbit, enabling continuous science data collection.

3.1.3 Cross-Sectional Areas and Notional Spacecraft Designs

Though CubeSats can nominally range in size from 0.5U to 27U, a discrete sampling of common dimensions, masses, and volumes were considered rather than attempt a continuous spectrum across all three dimensions, since many of the “in between” cases are not currently supported by dispenser technology. A notional set of spacecraft configurations considered in this study is given in Table 2. The clear blue circular area on each configuration is meant to represent an instrument boresight, since solar remote sensing instruments will likely need to point a boresight at the sun. The dark blue areas represent solar panels, and all spacecraft are shown in a deployed configuration.

Eq. 1 is the acceleration vector acting on the spacecraft due to atmospheric drag, and it is a governing equation for this analysis. This equation will be discussed in more detail in Section 3.4, but it is introduced here to show how the drag is directly affected by

Table 2: Notional spacecraft configurations.

Configuration	Specifications	Configuration	Specifications
	#1 Low Drag: 0.5U High Drag: 2.5U Mass: 0.66 kg Volume: 0.5U		#6 Low Drag: 2U High Drag: 15U Mass: 8 kg Volume: 6U
	#2 Low Drag: 1U High Drag: 3U Mass: 1.33 kg Volume: 1U		#7 Low Drag: 2U High Drag: 19U Mass: 8 kg Volume: 6U
	#3 Low Drag: 1U High Drag: 9U Mass: 4 kg Volume: 3U		#8 Low Drag: 3U High Drag: 13U Mass: 4 kg Volume: 3U
	#4 Low Drag: 2U High Drag: 5U Mass: 2.66 kg Volume: 2U		#9 Low Drag: 3U High Drag: 14U Mass: 8 kg Volume: 6U
	#5 Low Drag: 2U High Drag: 10U Mass: 5.33 kg Volume: 4U		

the cross-sectional area and mass of the spacecraft, given as A and m respectively in Eq. 1. Larger areas and smaller masses will increase the acceleration acting on the spacecraft from drag, and vice versa.

$$\mathbf{a}_{\text{drag}} = \left(-\frac{1}{2} \frac{C_D A}{m} \rho \right) (v_{\text{rel}})^2 \hat{\mathbf{v}}_{\text{rel}} \quad (1)$$

Fig. 9 shows the distribution of configurations as a comparison of high to low drag ratios vs. mass, and each volume is color-coded as well. The distribution of CubeSats in Table 2 and Fig. 9 were chosen to balance practicality, the depth available for an instrument, minimal deployments, and a variety of drag ratios, since a larger ratio will decrease the time needed for the two spacecraft to separate, but will also shorten the overall mission length.

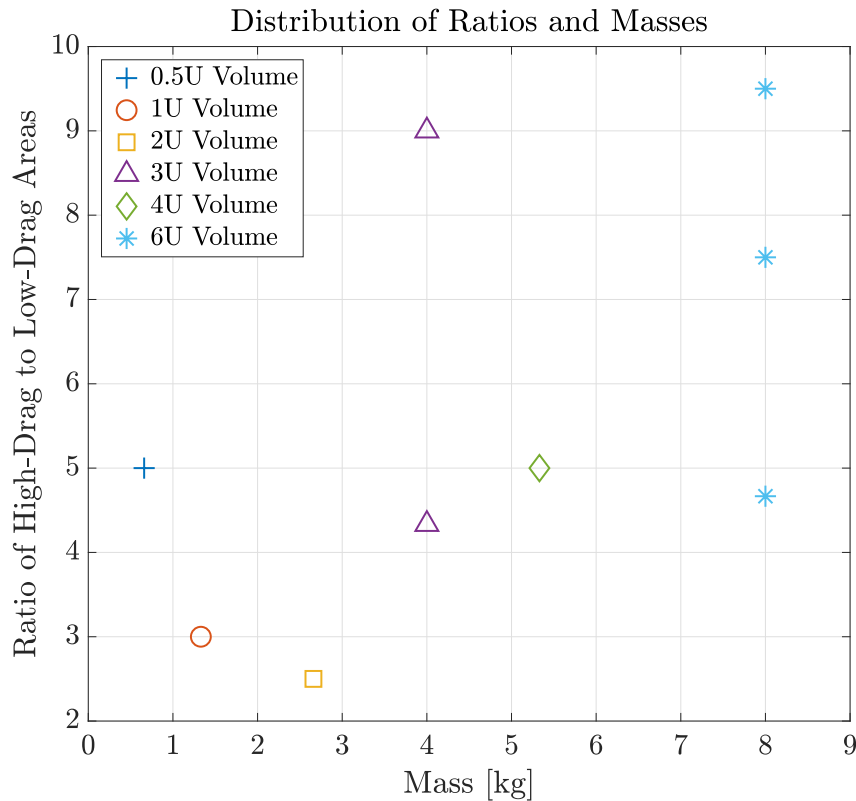


Figure 9: Distribution of notional CubeSat configurations showing the variation of drag ratios, masses, and volumes.

3.1.4 Body Frame Coordinate Axis Definition

As shown in Fig. 10, the body axes of the spacecraft are chosen such that the +X axis is always colinear with the instrument boresight, and the instrument boresight is always pointed in the same direction as the solar panels, which is good practice for solar observations. The +Z axis points out the “top” of the spacecraft, and the +Y axis completes the right-handed coordinate frame set.

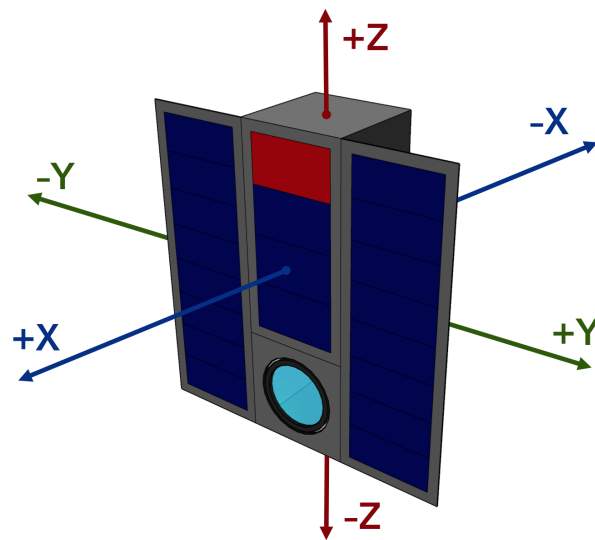


Figure 10: Body axes definition as shown on a sample CubeSat. Importantly, the +X direction is always pointed colinear with the instrument boresight.

3.1.5 Selection of Solar Minimum and Solar Maximum Conditions

Since increased solar activity has an impact on the density of the upper atmosphere due to atmospheric heating, I chose one solar minimum period and one solar maximum period to use as a baseline for this analysis. Fig. 11 shows the history of the $f_{10.7}$ cm radio flux since 1947, which illustrates the 11-year solar cycle variations. During solar minimum periods the $f_{10.7}$ values are fairly consistent, but the solar maximum periods have a wider variation with each cycle. For solar minimum, I used data from 2008 to 2010 shown near ②

in Fig. 11, and for solar maximum I used data from 1989 to 1991, shown near ①. For the solar maximum period, I chose the period at ① because it is not as high as the period from 1957 to 1959, nor is it as low as the most recent period of 2013 to 2015. In other words, it splits the difference between the two extremes of solar maxima periods that are present in the historical record. The values in Table 3 show typical values from the two datasets; these values are used in later analysis when comparing atmospheric density models.

Table 3: Range of $f10.7$ values and A_p values for the specific solar maximum and solar minimum periods used in this analysis. Note that $f10.7$ values are measured in solar flux units (sfu), where one sfu is equal to 10^{-22} W/m²/Hz.

	Solar Maximum 1989 to 1991	Solar Minimum 2008 to 2010
Range of $f10.7$ Flux	151.49 to 222.49 sfu	60.20 to 74.42 sfu
Mean Daily A_p Index	19.47	6.90

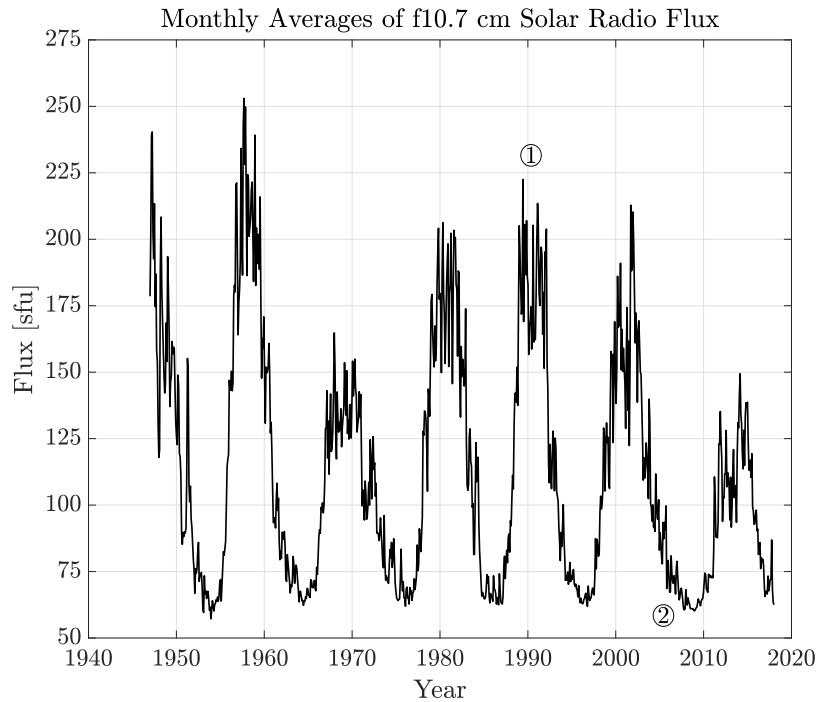


Figure 11: History of $f10.7$ cm radio flux, illustrating the 11-year solar cycle. Solar minima have fairly consistent values, but maxima have varied in intensity [32].

3.2 Two-Body Propagator

To characterize the orbital profile for the various cases studied, I wrote a two-body propagator in MATLAB and used the `ode45` integrator to determine the behavior based on a classic Newton's 2nd Law model. A similar analysis could be accomplished with a tool like Systems Tool Kit (STK) or the General Mission Analysis Tool (GMAT), though for this work I chose to start from first principles to have more control over each parameter. In the future, it would be interesting to compare the results of this analysis with STK or GMAT as an additional validation of the model.

Integrating the equations of motion with `ode45` requires that we define an initial state vector based on the classical orbital elements of the ISS orbit. We can use the orbital elements to create an initial position and velocity vector in the perifocal (PQW) frame, then use a rotation matrix to convert these vectors to an Earth-centered inertial (IJK) frame. The PQW frame is centered on the Earth with its principal axis \hat{p} pointed at periapsis of the orbit, the second vector \hat{q} in the same plane as the orbit pointed 90° past periapsis in the direction of orbital motion, and the third vector \hat{w} represents the angular momentum vector, oriented to complete the right-handed coordinate frame. Once we have the position vector in the IJK frame, we use this initial state to propagate the motion. Table 4 outlines an algorithm that is used to convert the classical orbital elements to a position-velocity state vector [5, 33]. The following orbital parameters are used in Table 4:

- Ω is the right ascension of the ascending node
- ω is argument of perigee
- i is the inclination of the orbit with respect to Earth's equator
- p is the semiparameter or semi-latus rectum, defined as the vertical distance from one focus of the orbit to the orbital path, parallel with the semi-minor axis

- a is the semi-major axis of the orbital ellipse
- e is the eccentricity of the orbit
- ν is the true anomaly of the orbit
- μ_{\oplus} is the gravitational parameter for the Earth as defined previously in Table 1

Table 4: Algorithm 1 shows how to convert classical orbital elements to position and velocity vectors in an Earth-centered inertial space. Specific equations are given in Eqs. 2 to 7.

Algorithm 1—Convert Orbital Elements to \vec{r} and \vec{v} Vectors

-
- 1: Create rotation matrix to convert PQW frame to IJK frame using Ω , ω , and i
 - 2: Compute the semiparameter with $p = a \cdot (1 - e^2)$
 - 3: Assemble the initial position vector \mathbf{r}_{PQW} in PQW coordinates using p , e , and ν
 - 4: Assemble the initial velocity vector \mathbf{v}_{PQW} in PQW coordinates using μ_{\oplus} , p , e , and ν
 - 5: Use the rotation matrix from Step 1 to rotate \mathbf{r}_{PQW} and \mathbf{v}_{PQW} to the IJK frame.
-

The rotation matrix Q to convert from PQW to IJK is given by:

$$Q_{\text{PQW}}^{\text{IJK}} = \begin{bmatrix} \cos \Omega \cos \omega - \sin \Omega \sin \omega \cos i & \sin \Omega \cos \omega + \cos \Omega \sin \omega \cos i & \sin \omega \sin i \\ -(\cos \Omega \sin \omega) - \sin \Omega \cos \omega \cos i & -(\sin \Omega \sin \omega) + \cos \Omega \cos \omega \cos i & \cos \omega \sin i \\ \sin \Omega \sin i & -(\cos \Omega \sin i) & \cos i \end{bmatrix} \quad (2)$$

After computing the semiparameter with the equation as given in Table 4, we can compute the position and velocity vectors in the PQW frame with Eqs. 3 and 4.

$$\mathbf{r}_{\text{PQW}} = \begin{bmatrix} \frac{p \cos \nu}{1 + e \cos \nu} \\ \frac{p \sin \nu}{1 + e \cos \nu} \\ 0 \end{bmatrix} \quad (3)$$

$$\mathbf{v}_{\text{PQW}} = \begin{bmatrix} -\sqrt{\frac{\mu_{\oplus}}{p}} (\sin \nu) \\ \sqrt{\frac{\mu_{\oplus}}{p}} (e + \cos \nu) \\ 0 \end{bmatrix} \quad (4)$$

Then we can compute the initial state vector in the IJK frame with:

$$\mathbf{r}_{\text{IJK}} = Q_{\text{PQW}}^{\text{IJK}} \mathbf{r}_{\text{PQW}} \quad (5)$$

$$\mathbf{v}_{\text{IJK}} = \mathbf{Q}_{\text{PQW}}^{\text{IJK}} \mathbf{v}_{\text{PQW}} \quad (6)$$

Now we can define the initial state vector as:

$$\mathbf{X}_0 = \begin{bmatrix} \mathbf{r}_{\text{IJK}} \\ \mathbf{v}_{\text{IJK}} \end{bmatrix} \quad (7)$$

3.3 Propagation with ode45

With the initial state defined, we can begin to propagate our equations of motion using `ode45`, which uses a variable time step and an optional tolerance value, which can be set as needed for each individual simulation run. The function that is passed to `ode45` has the basic form as shown in Table 5, which is used for all analysis cases. Once the position vector r is defined, we use the gravitational parameter and the universal law of gravitation to determine the acceleration of the spacecraft due to gravity:

$$\ddot{r}_{x, \text{grav}} = -\frac{\mu_{\oplus} \cdot r_x}{r^3} \quad \ddot{r}_{y, \text{grav}} = -\frac{\mu_{\oplus} \cdot r_y}{r^3} \quad \ddot{r}_{z, \text{grav}} = -\frac{\mu_{\oplus} \cdot r_z}{r^3} \quad (8)$$

Table 5: Algorithm 2 showing the iteration steps that are passed to `ode45`.

Algorithm 2—Propagate the Orbit with ode45

- | | |
|----|---|
| 1: | Compute the magnitude of the position vector with $ \mathbf{r} = r = \sqrt{r_x^2 + r_y^2 + r_z^2}$ |
| 2: | Compute second derivatives of the position to find the gravitational acceleration. |
| 3: | Find the atmospheric density based on the position vector. |
| 4: | Compute the velocity vector relative to atmospheric rotation. |
| 5: | Compute acceleration vector of the drag based on the relative velocity vector. |
| 6: | Add drag and gravitational acceleration vectors. |
| 7: | Return and integrate $\dot{\mathbf{X}}$, then repeat the process. |

Step 3 in Algorithm 5 involves finding the atmospheric density based on the position of

the spacecraft. I have compared two different density models in this analysis in order to investigate the variation in results due to atmospheric density.

3.3.1 Density Model—Exponential

The first method to compute the density ρ is an empirically derived exponential model that is valid in the atmosphere below 500 km, which correlates well with the orbits I am considering [34]. This model, which was developed by the Australian Space Weather Agency, is advantageous because it makes allowances to adjust the values for A_p (the geomagnetic index) and the $f10.7$ index (the solar radio flux at 10.7 cm), which are correlated to the strength of the solar cycle and have a direct impact on atmospheric density. To choose values, I looked at the solar maximum and solar minimum periods defined previously, then used appropriate values from Table 3 for the analysis. For solar maximum, I used $f10.7 = 222.50$ sfu and $A_p = 19.47$. For solar minimum I used $f10.7 = 60.20$ sfu and $A_p = 6.90$. In general, the A_p index varies between approximately 0 and 25 during the solar cycle, and the $f10.7$ index varies between approximately 60 and 300, so these values are in family with expected trending [35, 36]. Next we compute the atmospheric temperature T and the molecular mass m_{mol} as a function of altitude h (which is simply $r - R_{\oplus}$), and the scale height H , which is then used to determine the density ρ at a given altitude h .

$$\begin{aligned}
 T &= 900 + 2.5(f10.7 - 70) + 1.5A_p && \text{[K]} \\
 m_{\text{mol}} &= 27 - 0.012(h - 200) && \text{[unitless]} \\
 H &= \frac{T}{m_{\text{mol}}} && \text{[km]} \\
 \rho &= (6 \times 10^{-10}) e^{-(h-175)/H} && \text{[kg/m}^3\text{]}
 \end{aligned} \tag{9}$$

This model is often the preferred method for analysis since it allows for faster simulation

run-times. To account for variations in location, the density must be computed for every iteration of the propagator, so the simple relationships in Eq. 9 result in faster computations throughout the propagator.

3.3.2 Density Model—Naval Research Laboratory’s MSISE-00 Model

Over the past few decades, the United States Naval Research Lab has developed an empirical atmospheric model that estimates the temperature and density of the major molecular components of the atmosphere, from the ground to 1000 km [37]. The earlier versions of this model combined data from the Middle Atmosphere Program handbook for altitudes below 72.5 km [38], as well as data from the National Meteorological Center for data below 20 km. For data above 72.5 km, the MSIS model has its foundations from previous models such as CIRA-86, but it has been revised with data from Space Shuttle flights, sounding rockets, satellite drag, and other sources of new data [39]. MSIS stands for Mass-Spectrometer-Incoherent-Scatter, and the “E” indicates that this model includes data from the surface of the Earth up through the exosphere at 1000 km. Finally, the “00” indicates that this is the model from the year 2000; previously there were MSIS models from 1986 and 1990 [39].

This model provides precise estimates for the atmospheric density that are based on altitude, latitude, longitude, the time of year, plus the same A_p and $f_{10.7}$ indexes that were discussed previously. Conveniently, MATLAB provides a function for this model called `atmosnrlmsise00`, which will pull data from the model when given the correct parameters [40]. The function takes the following inputs: altitude, latitude, longitude, year, day of year, seconds in UTC, 81-day average $f_{10.7}$ centered on the day of year, the previous day’s $f_{10.7}$

value, and a 7-value array of recent A_p indexes. One advantage of this model is that it may get closer to a “truth” value for the density since it accounts for many more variables, though this comes with a cost—the expanded capabilities makes it more difficult to implement, and I’ve found that it significantly increases the computation time in MATLAB. Regardless, since the MSIS model has become a standard in the community, it has still been worthwhile to execute as many simulations as possible with this model.

Calculating the inputs for the MSIS model is non-trivial, and so I will include a discussion of that process here. While other parts of the propagator are computationally quick, this is one place where it would be advantageous to use STK for the propagation since the NRLMSISE-00 model is included and the MATLAB version that I wrote is computationally tedious. The first input to the model is the altitude, which for any given point in the orbit is simply the magnitude of the current position vector minus the radius of the Earth. Next we need the geodetic latitude and longitude, which is somewhat complex to derive from the position vector. The algorithm for this process is shown in Table 6/Algorithm 3.

Step 1 of Algorithm 3 is dependent on a specified time period. Since the NRLMSISE-00 model uses data going back to 1947, it requires that you supply a particular epoch so it can pull the appropriate data. To compare solar minimum and solar maximum conditions, I chose to center the simulations around two time periods, one starting on February 1, 2008 and one starting on February 1, 1989, which correspond to solar minimum and solar maximum respectively. The reason for starting in February is somewhat arbitrary, though it was chosen over January 1 to allow for some “past” data to exist within a calendar year, since the data available is divided by calendar year. Once the UTC time is converted to Julian date, we use Eq. 10 to calculate the Greenwich Mean Sidereal Time, θ_{GMST} . This

Table 6: Algorithm 3 shows how to convert an Earth-centered inertial (ECI) position vector to geodetic latitude and longitude, which is needed to use the NRLMSISE-00 model atmospheric model.

Algorithm 3—Convert ECI position vector to latitude/longitude

- 1: Convert the current integration time step to Julian date from UTC, where the simulation time is correlated to a solar minimum period (starting in 2008) or solar maximum period (starting in 1989).
- 2: Convert the Julian date to the Greenwich Mean Sidereal Time, θ_{GMST} , defined as the time between the vernal equinox line and the 0° longitude line. This time value can then be converted into an angle.
- 3: Using θ_{GMST} as an input, convert the ECI position vector to the Earth-centered Earth-fixed (ECEF) frame.
- 4: Use the z component of the ECEF position vector and the eccentricity of the Earth to find the geodetic latitude, ϕ_{gd} which requires iteration until a tolerance value is surpassed.
- 5: Convert the x and y components of the ECEF position vector to longitude, λ .

equation is applicable for dates between 1901 to 2199, but not beyond these bounds since the constants in Eq. 10 do not account for centuries that are evenly divisible by 400 [5]. Since θ_{GMST} is calculated in seconds, I also convert the value to degrees by dividing θ_{GMST} by 240, since there are 240 seconds per degree [5].

$$t = \frac{\text{Time in JD} - 2,451,545.0}{36,525}$$

$$\theta_{\text{GMST}} = 67,310.54841^{\text{s}} + (876,600^{\text{h}} + 8,640,184.812866^{\text{s}}) t + 0.093104t^2 - (6.2 \times 10^{-6}) t^3 \quad (10)$$

Step 3 of Algorithm 3 requires using θ_{GMST} to convert the ECI position vector to an ECEF position vector, which will enable a later conversion to latitude and longitude. This is accomplished with a relatively simple rotation matrix:

$$\mathbf{r}_{\text{ECEF}} = \mathbf{Q}_{\text{ECI}}^{\text{ECEF}} \mathbf{r}_{\text{ECI}}$$

$$\mathbf{r}_{\text{ECEF}} = \begin{bmatrix} \cos(\theta_{\text{GMST}}) & \sin(\theta_{\text{GMST}}) & 0 \\ -\sin(\theta_{\text{GMST}}) & \cos(\theta_{\text{GMST}}) & 0 \\ 0 & 0 & 1 \end{bmatrix} \mathbf{r}_{\text{ECI}} \quad (11)$$

Converting \mathbf{r}_{ECEF} to latitude requires iteration because the Earth is not a perfect sphere, and therefore the geodetic latitude of a satellite's position is often not the same if we were to drop a perpendicular vector from the satellite to the ground [5]. The set of equations used to compute the geodetic latitude are given in Eqs. 12 to 15, given the radius of the Earth as $R_{\oplus} = 6378.1363$ km, the eccentricity of the Earth as $e_{\oplus} = 0.081819221456$, and define r_{δ} as the equatorial projection of the satellite's IJK (ECEF) position vector.

$$r_{\delta} = \sqrt{(r_I)^2 + (r_J)^2} \quad (12)$$

$$\delta = \tan^{-1} \left(\frac{r_K}{r_{\delta}} \right) \quad (13)$$

The value δ is the declination angle, and since declination is the same as the *geocentric* latitude, δ should be close to the geodetic latitude and can be used as an initial guess in the iteration, such that $\delta \approx \phi_{gd}$. The following two equations were iterated until the difference between the “current” and “previous” values of ϕ_{gd} was less than a specified tolerance of 0.1. The tolerance value could certainly be varied, but this value seemed to produce accurate results while not increasing the computation time significantly. The parameter C_{\oplus} is an intermediate geometric value (it is the radius of curvature in the meridian of an ellipse [5]), and has no special meaning here except that it is used to compute ϕ_{gd} .

$$C_{\oplus} = \frac{R_{\oplus}}{\sqrt{1 - e_{\oplus}^2 \sin^2(\phi_{gd})}} \quad (14)$$

$$\phi_{gd} = \tan^{-1} \left(\frac{r_K + C_{\oplus} (e_{\oplus})^2 \sin(\phi_{gd})}{r_{\delta}} \right) \quad (15)$$

The last step of Algorithm 3 is to calculate the longitude, which is fairly straightforward since geodetic and geocentric longitude are the same:

$$\lambda = \tan^{-1} \left(\frac{r_J}{r_I} \right) \quad (16)$$

Finally, now that I have the position vector converted to latitude and longitude, I can use the MATLAB function `atmosnrlmsise00` to query the NRLMSISE-00 model and find the atmospheric density for the specific position vector and time. This density value is used to compute the acceleration vector that results from atmospheric drag. Section 4 includes a comparison plot of altitude vs. density for both models at solar minimum and solar maximum conditions to illustrate why both models were considered; see Fig. 19.

3.4 Adding the Drag Force

When we compute the drag vector, we have to consider the fact that the atmosphere is also rotating with the Earth, so we need to calculate the velocity vector relative to atmospheric rotation [5]. Note that this relationship assumes that the atmosphere rotates at the same rate as the Earth, and that any effects from thermospheric winds are ignored. In Eq. 17, $\boldsymbol{\omega}_{\oplus}$ is the angular rotational velocity vector of the Earth, given by $\boldsymbol{\omega}_{\oplus} = [0 \ 0 \ 7.292115 \times 10^{-5}]'$ rad/s.

$$\mathbf{v}_{\text{rel}} = \dot{\mathbf{r}} - \boldsymbol{\omega}_{\oplus} \times \mathbf{r} \quad (17)$$

Now we can compute the acceleration vector for the drag given in Eq. 18, using a coefficient of drag of $C_D = 2.2$, with mass m and cross-sectional area A based on the particular case we

are considering. Note that this is the same equation given previously in Eq. 1, reproduced here for convenience.

$$\mathbf{a}_{\text{drag}} = \left(-\frac{1}{2} \frac{C_D A}{m} \rho \right) (v_{\text{rel}})^2 \hat{\mathbf{v}}_{\text{rel}} \quad (18)$$

Historically, using a value of 2.2 for the coefficient of drag has been considered standard practice for flat-plate models of spacecraft in low Earth orbit [5]. This value became the standard because our knowledge of gas-surface interactions at altitudes above 150 km was not well known. We now understand these issues better, in particular the effect of atomic oxygen that is adsorbed on spacecraft surfaces, which directly affects the coefficient of drag [41]. Recently, however, researchers have used spacecraft data and an our increased understanding of the fundamental physics that control these processes to modify the estimates of the coefficient of drag, particularly above 150 km. In one case, it is estimated that the MSIS-90 model over-estimates the atmospheric drag by 15% because of inaccurate estimates of C_D [41]. In an effort to reduce the number of variables under consideration, I will continue to use the value of $C_D = 2.2$, with the understanding that some of the density estimates above 150 km may be unrealistically high.

When we are concerned with the three-dimensionality of the spacecraft (i.e. anything except a strict ram-facing case), we need to do a small calculation to find the value for A . In this case, I took the dot product of each face's area with the unit vector of the velocity, since that will be the portion of the face that is affected by the atmospheric drag. Once this is done for all six faces of the CubeSat, they are summed to get the effective cross-sectional area, as shown in Eq. 19. This equation includes a sample area matrix for spacecraft configuration

#3—notice that the values in the matrix correspond to the body frame coordinates as shown in Section 3.1.4.

$$A_i \cdot \hat{v} = \begin{bmatrix} 0.09 & 0.00 & 0.00 \\ -0.09 & 0.00 & 0.00 \\ 0.00 & 0.03 & 0.00 \\ 0.00 & -0.03 & 0.00 \\ 0.00 & 0.00 & 0.01 \\ 0.00 & 0.00 & -0.01 \end{bmatrix} \cdot \begin{bmatrix} v_x \\ v_y \\ v_z \end{bmatrix} \rightarrow A = \sum_{i=1}^6 A_i \cdot \hat{v} \quad (19)$$

Additionally, Fig. 12 shows how the effective cross-sectional area changes over a single orbit for each spacecraft configuration when solar-pointed. One interesting outcome from this plot is that the high-drag profile is not actually the largest cross-sectional area for a given spacecraft—for example, Case 7's high-drag profile is the solar panel face with an area of 1900 cm², but the largest value in Fig. 12 for Case 7 is actually 1997 cm² because a slightly off-pointed attitude results in a larger cross-sectional area.

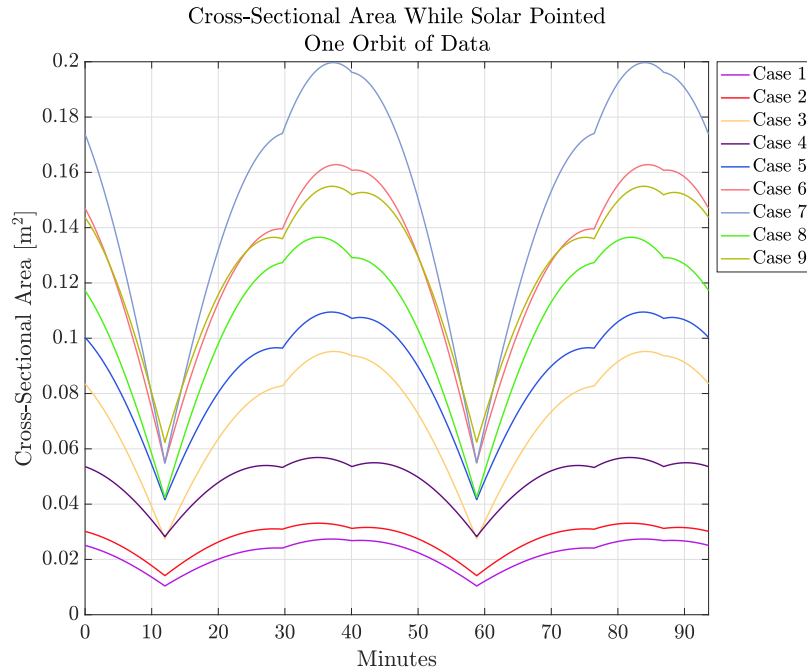


Figure 12: The cross-sectional area changes over a single orbit for each spacecraft configuration, and the high-drag profiles used in my analysis are actually a bit smaller than the attitude for the highest drag.

One caveat with this method is that it does not account for partial faces that are self-shadowed by the solar panels from the incoming atmospheric particles, as illustrated in Fig. 13. Essentially, parts of the spacecraft body that are blocked by the solar panels are included in the area calculation of Eq. 19, so the results shown will be a worst-case scenario and may predict a shorter mission lifetime than expected. This issue is discussed further in Section 5.

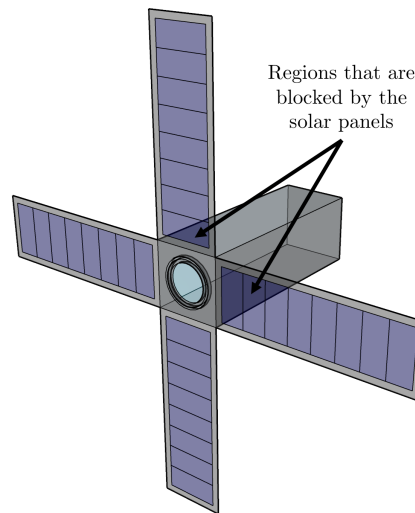


Figure 13: A sample spacecraft configuration showing how parts of the spacecraft body may be self-shadowed by the solar panels (in this view, the spacecraft would be flying directly out of the page). This is discussed further in Section 5.

From Eq. 18, note that the quantity $\frac{C_D A}{m}$ is the inverse of the ballistic coefficient (BC), which characterizes how well a body can overcome drag; higher ballistic coefficients will correlate to a decrease in the drag force experienced by the object. For example, in a normal atmosphere a bullet would have a high BC, while a beach ball would have a low BC. Since our drag equation uses $1/BC$, we would expect a small value of $\frac{C_D A}{m}$ for heavy CubeSats with small ram-facing cross-sectional areas and vice versa. The ballistic coefficients for each spacecraft configuration are given in Table 7, and they give a sense of how easily a particular configuration can change its location in the orbit via drag.

Table 7: Inverse ballistic coefficients (BC, defined as $\frac{C_D A}{m}$) for each spacecraft configuration that were shown in Table 2, using $C_D = 2.2$. The last column gives the high drag to low drag BC ratio, which gives a sense of how easily this configuration will be able to change its location in the orbit using differential drag (higher BC would separate more easily).

ID #	Mass	Low Drag Area	High Drag Area	High Drag BC	Low Drag BC	BC Ratio (High-Low)
1	0.66 kg	0.005 m ²	0.025 m ²	0.0833	0.0167	5.0
2	0.66 kg	0.01 m ²	0.03 m ²	0.0496	0.0165	3.0
3	2.66 kg	0.02 m ²	0.05 m ²	0.0495	0.0055	9.0
4	5.33 kg	0.02 m ²	0.10 m ²	0.0414	0.0165	2.5
5	4 kg	0.01 m ²	0.09 m ²	0.0413	0.0083	5.0
6	4 kg	0.03 m ²	0.13 m ²	0.0413	0.0055	7.5
7	8 kg	0.02 m ²	0.15 m ²	0.0523	0.0055	9.5
8	8 kg	0.01 m ²	0.14 m ²	0.0715	0.0165	4.3
9	8 kg	0.02 m ²	0.19 m ²	0.0385	0.0083	4.7

The last step of the propagator is to add the drag acceleration to the gravitational acceleration and then return the derivative of the state vector, as shown in Eqs. 20 and 21. This algorithm is used for all of the following analysis and results unless otherwise stated. If higher order effects were included in this analysis, they would be linearly added at this step.

$$\begin{aligned}\ddot{r}_x &= \ddot{r}_{x, \text{grav}} + a_{x, \text{drag}} \\ \ddot{r}_y &= \ddot{r}_{y, \text{grav}} + a_{y, \text{drag}} \\ \ddot{r}_z &= \ddot{r}_{z, \text{grav}} + a_{z, \text{drag}}\end{aligned}\tag{20}$$

$$\dot{\mathbf{X}} = \begin{bmatrix} \dot{\mathbf{r}} \\ \ddot{\mathbf{r}} \end{bmatrix}\tag{21}$$

The parameters passed in to `ode45` can vary depending on the analysis being performed. I run a coarse analysis by only computing the new state vectors for a few weeks of time, and use the results to debug and tweak the simulation as needed. To obtain the results shown in the next section, a variable time step was used to ensure the simulation has enough

fidelity to model the behavior as closely as possible. Additionally, all simulations use a 10^{-6} relative and absolute tolerance for the `ode45` integrator; this value until was adjusted until a tolerance level was found that balanced computational time with fidelity of the results.

4 Results and Discussion

As stated previously, the purpose of this project is to determine the feasibility of using a constellation of two CubeSats to conduct continuous solar science. I have made the following assumptions and constraints for this project:

1. Both CubeSats will be deployed at the same time from the ISS, therefore both spacecraft will have the same initial state vector.
2. Though the ISS is generally at an altitude of approximately 405 km, orbits between 400 and 500 km will be considered since the Cygnus resupply vehicle provides an opportunity to deploy above the ISS up to 500 km.
3. During the initial separation, the lead spacecraft will maintain its low-drag face pointed in the ram direction, and the follower spacecraft will maintain its high-drag face pointed in the ram direction. The time to separate to 180° apart will be computed.
4. After the initial separation, both spacecraft will maneuver such that the instrument boresight (and therefore the solar panels) are always solar-pointed.
5. Nine separate spacecraft configurations are considered; see Table 2 for details of the nine configurations.

With these assumptions in mind, we can look at the results of the simulations and determine whether this is a feasible mission concept. As I was exploring the trade space for this mission concept, I expected that the mission would be most achievable at higher altitudes with solar minimum conditions. At solar minimum, the atmospheric density value is smaller, so while the two spacecraft would take longer to separate in their orbit, the overall mission duration

would increase. Despite the longer separation time, an extended data collection period would be attractive from a science perspective. Similarly, I expected that some configurations would be infeasible, or that the time needed to separate the two spacecraft would be so large that the science period would be impractically short. The following sections will go into more detail on the results of the simulations.

4.1 Baseline Simulation

Since there is a large trade space associated with this mission concept, I first assessed the overall concept by simulating the altitude decay of all nine spacecraft configurations for a single set of parameters, which I consider a baseline for other analysis scenarios:

- Starting Altitude: 450 km
- Density Model: NRLMSISE-00
- Time Period: Solar Minimum (2008 to 2010)

These parameters describe a set of conditions that produce feasible results for all spacecraft configurations. As shown in Fig. 14, each spacecraft pair has a mission length exceeding 500 days, with the leader spacecraft deorbiting later than the follower. The orbit propagation is stopped when each spacecraft reaches an altitude of 100 km above the surface of the Earth. These plots have all variables held constant except the spacecraft configuration, so we can clearly see which configurations extend the mission lifetime the most and which ones deorbit the quickest.

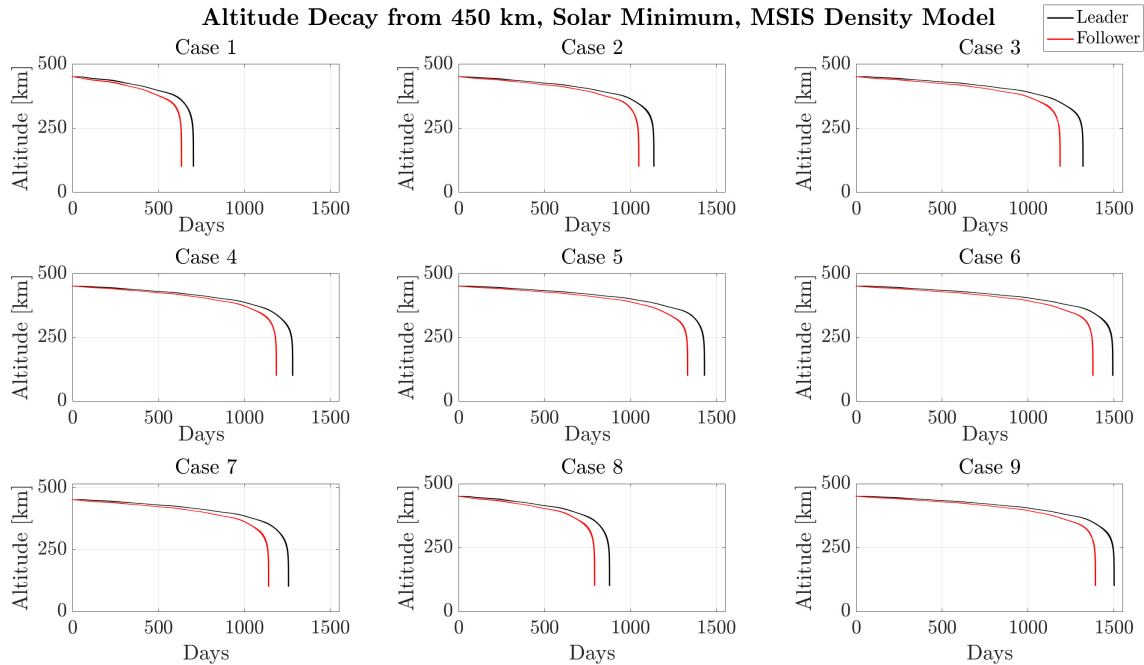


Figure 14: Summary of all nine spacecraft configurations, with the simulation run for a baseline case of 450 km starting altitude, during solar minimum conditions, with the MSIS density model. As a reminder, the configurations are as follows: Case 1 is 0.5U with 250 cm² solar panels, Case 2 is 1U with 300 cm² solar panels, Case 3 is 3U with 900 cm² solar panels, Case 4 is 2U with 500 cm² solar panels, Case 5 is 4U with 1000 cm² solar panels, Case 6 is 6U with 1500 cm² solar panels, Case 7 is 6U with 1900 cm² solar panels, Case 8 is 3U with 1300 cm² solar panels, and Case 9 is 6U with 1400 cm² solar panels.

Table 8: Separation time and mission duration for all nine spacecraft configurations as shown in the baseline simulation.

Configuration	Separation Time [days]	Mission Duration [days]
1	58.40	575.50
2	81.67	966.33
3	71.71	1114.29
4	93.84	1092.16
5	82.25	1250.75
6	79.28	1297.72
7	69.65	1071.35
8	64.03	727.17
9	85.83	1306.17

Additionally, Fig- 15 shows a zoomed-in annotation for the start of the simulation to

highlight where the two mission phases are stitched together. At the start of the simulation, the propagator is using parameters for the ram-pointing case, and it runs in this configuration until the angle between the two position vectors reaches 180° . Once this point is reached, the final state vector from the ram-pointing phase is used as the initial state vector for the solar-pointed propagator, which is clearly visible as a change in slope in Fig. 15. Note that the simulation shown in Fig. 15 is for a slightly different case than the baseline simulation—I chose to show a 400 km case instead of 450 km since the slope change is more obvious.

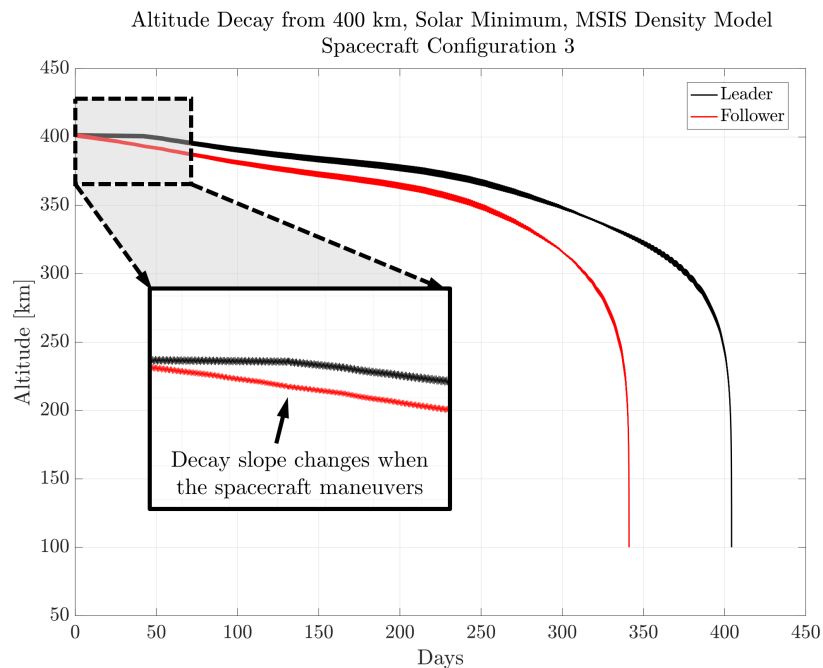


Figure 15: Altitude decay of spacecraft configuration #3, from 400 km altitude at solar minimum, simulation run with the MSIS model. In particular, this figure is included to show the slope change in the altitude that occurs when the spacecraft maneuvers after the two spacecraft have reached 180° of separation.

After the two spacecraft reach 180° separation, no attitude maneuvers are used to maintain this separation; the two CubeSats will continue to drift as shown in Fig. 16 unless a control algorithm is implemented to maintain their in-track position. From this plot it is difficult to discern how much time would be lost to having both spacecraft in eclipse, since

a small angular separation does not necessarily imply that both will be in eclipse at the same time. This is another place where an STK model could be helpful since the analysis is dependent on the angle between the two position vectors and the overall position of the constellation relative to the Sun. A more detailed discussion on this topic is included in Section 5.1.

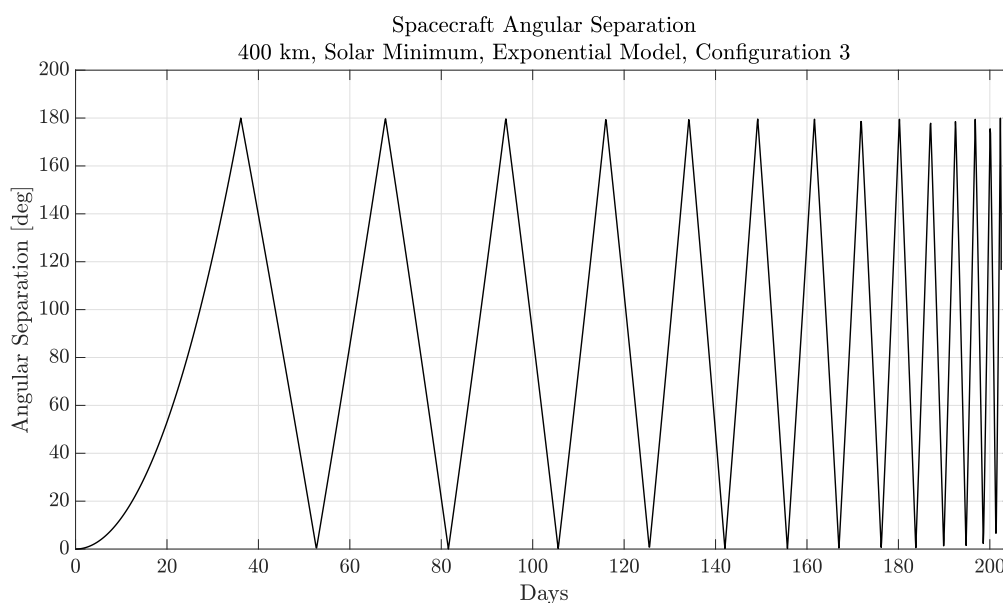


Figure 16: Angular separation of the two spacecraft for a simulation starting at 400 km, using the exponential density model, at solar minimum, for spacecraft configuration 3.

4.2 Mission Duration and Length of Commissioning Phase

The altitude decay plots shown in Figs. 14 and 15 are the initial results that I gathered from the simulations, and for each simulation I have an altitude decay plot that shows how the mission evolves—all of them have the same basic shape and behavior, just with different mission phase durations. These plots are difficult to glean insight from, and don't really show the full breadth of the trade space. Instead, Fig. 17 presents results from a larger set of data such that each point on the plot represents a single simulation run,

with the triangles representing solar minimum conditions and the circles representing solar maximum conditions. The points are also color coded to match the starting altitude of the simulation; black for 500 km, blue for 450 km, and red for 400 km. The x-axis shows the number of days each simulation takes to separate the two spacecraft to 180° , and the y-axis shows the subsequent mission length until the first CubeSat deorbits. In other words, the x-axis shows the length of the commissioning phase, and the y-axis shows the length of the prime mission phase.

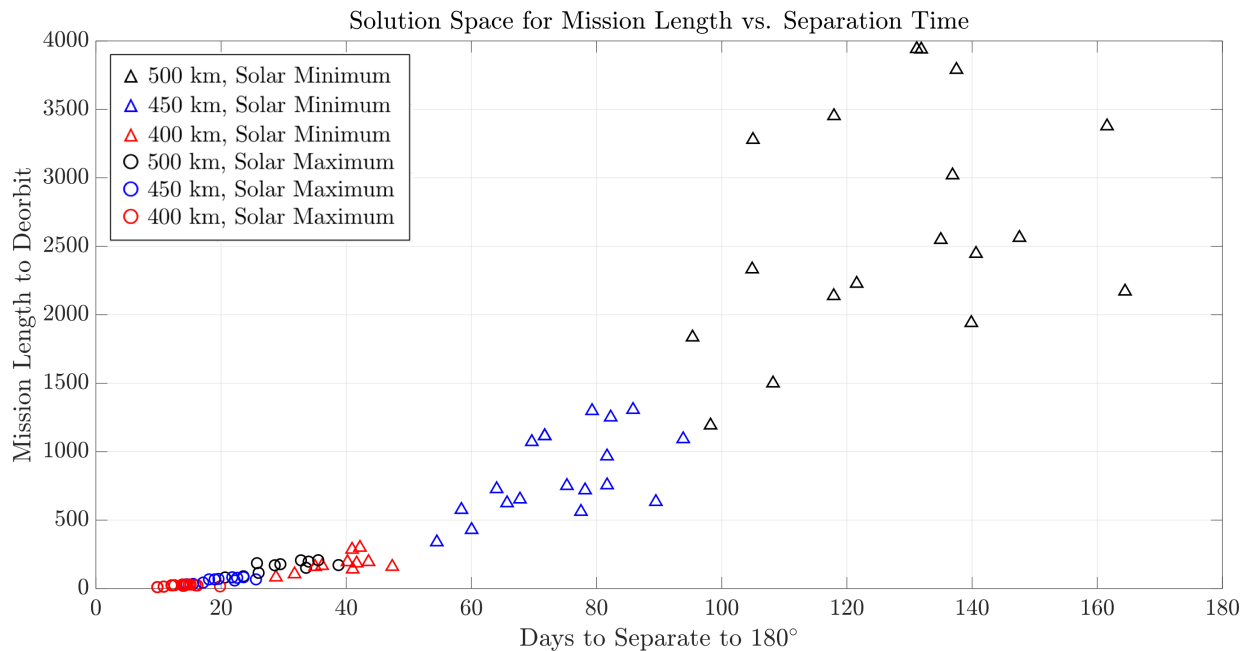


Figure 17: This plot explores the relationship between the length of the commissioning phase (shown on the x-axis) and the length of the prime mission phase (shown on the y-axis), for a variety of simulation input parameters. Each point represents a single simulation run, and both density models are included in this data.

From this plot, it is clear that missions at solar minimum provide longer overall mission lifetimes, and that higher starting altitudes also increase mission length. There is also a large difference between results from solar minimum and solar maximum conditions, which is a result that I did not anticipate. I expected some difference, but the dramatic

increase in mission length was a bit surprising. Considering the discussion in Section 3.4, it is possible that the MSIS model is miscalculating the density at higher altitudes, which could contribute to some error in these results. Regardless, even if the durations are lower than predicted by my propagator, they still present a viable solution space.

Fig. 18 shows a zoomed in portion of Fig. 17 to more clearly see the solar maximum results. The overall pattern of results is expected—higher altitudes produce longer mission lengths and vice versa. However, from this plot it is clear that all of the 400 km cases at solar maximum are likely infeasible. In some cases, the two spacecraft may spend 15 days separating to 180° but then the follower spacecraft deorbits only 29 days later. It is possible that this could still be a useful mission profile, but it is more likely that longer mission durations would be desirable.

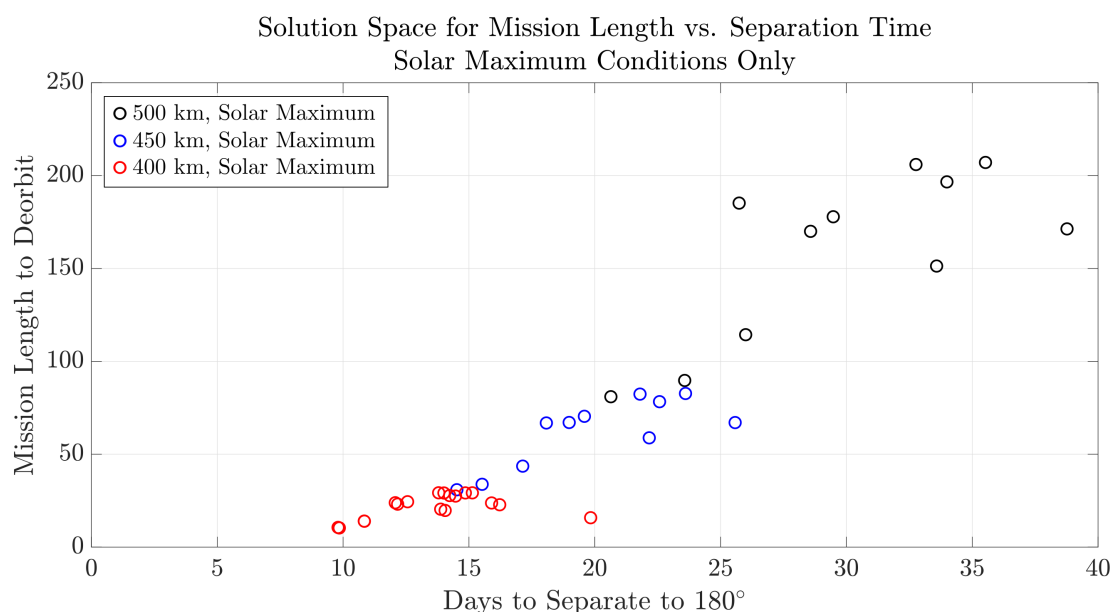


Figure 18: Zoomed in version of Fig. 17 to show the results for solar maximum conditions more clearly. As with solar minimum, the higher altitudes have longer mission lengths, though we see that all of the 400 km cases are likely too short to be feasible.

From Figs. 17 and 18, it is difficult to see how the density models compare, so the next

section will include results to illuminate those differences.

4.3 Comparing the Two Density Models

As discussed previously, the exponential density model from the Australian Space Weather Agency and the Naval Research Laboratory's MSISE-00 model were both used in this project. The exponential model is geographically homogeneous, i.e. it only considers the altitude above the surface and it has a simpler method for incorporating the $f_{10.7}$ and A_p indexes. On the other hand, the MSISE-00 model *does* account for geographical variation and it uses a more complex method to incorporate the $f_{10.7}$ and A_p indexes, though it may overestimate the density at higher altitudes as discussed in Section 3.4.

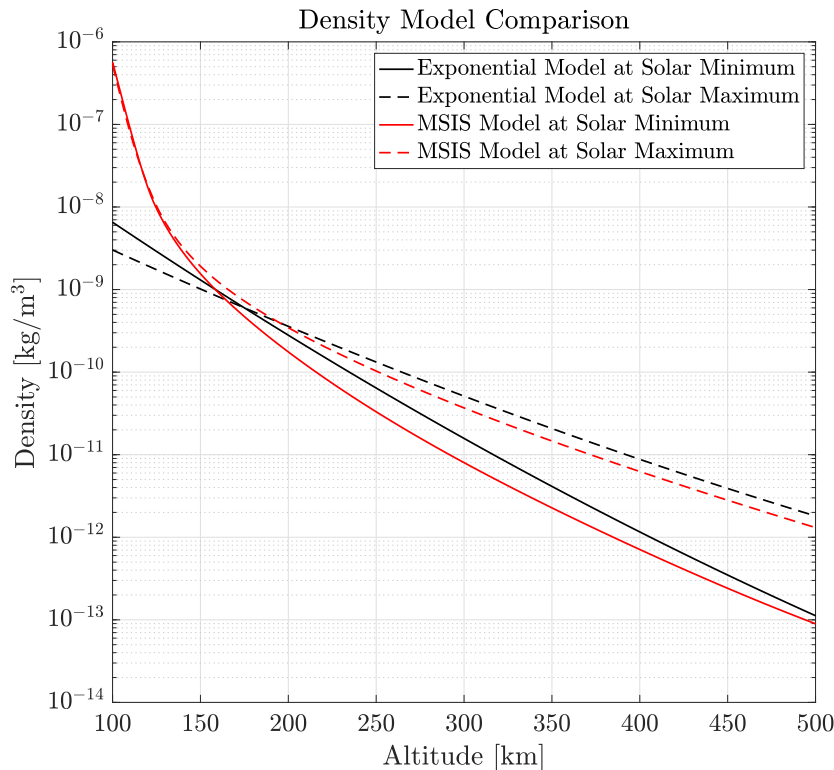


Figure 19: Comparison of the NRLMSISE-00 and Exponential density models for both solar maximum and solar minimum conditions.

Fig. 19 shows a comparison of the output of each model at solar minimum and solar maximum conditions. Above 150 km, the two models closely follow one another, with a percentage difference of approximately 64.4% around 260 km. Below 150 km the two models deviate significantly, but at these low altitudes the spacecraft is rapidly deorbiting and so the cumulative effect will be small. The order-of-magnitude difference between solar minimum and solar maximum conditions at higher altitudes is the cause of the dramatic differences in mission length for the two different solar conditions.

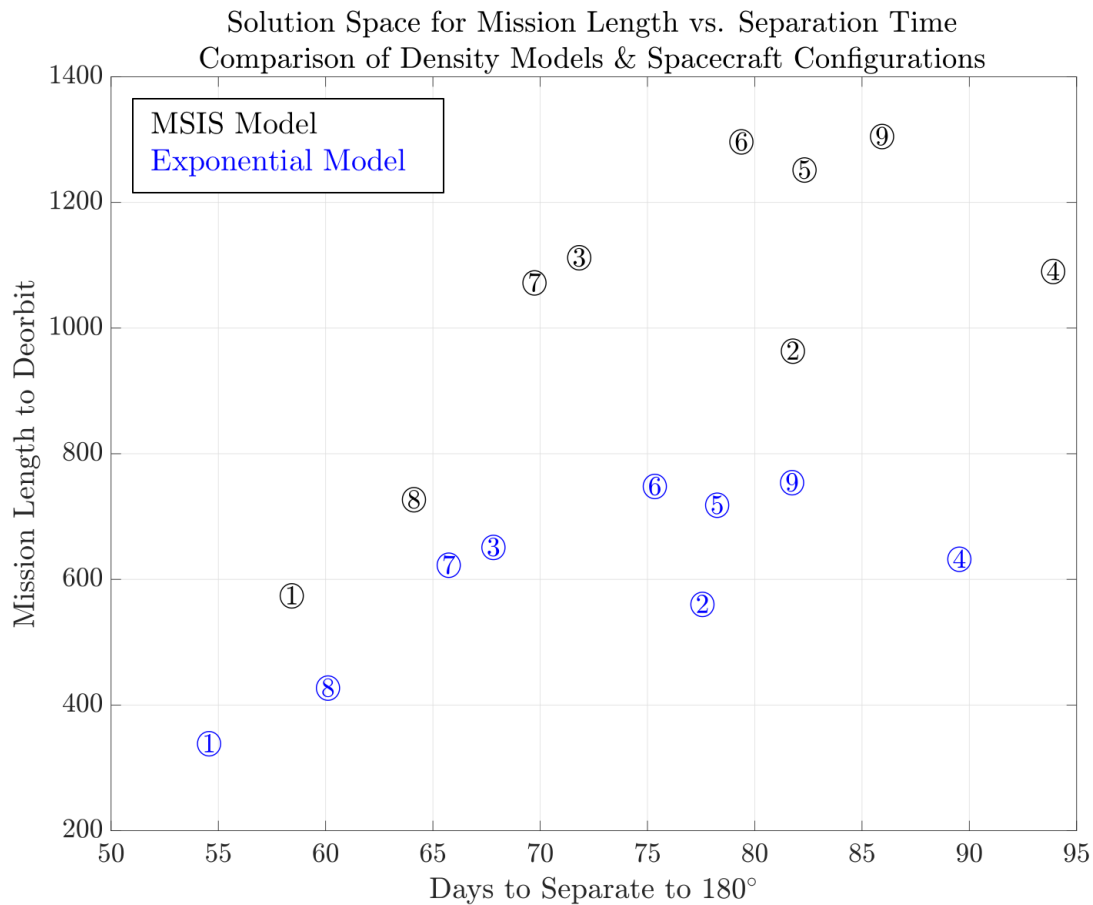


Figure 20: This plot shows the same “blue triangle” data from Fig. 17, which is the simulations run at 450 km during solar minimum, but this plot differentiates between the two density models. Each number indicates the spacecraft configuration for that simulation.

In order to better understand how the density model affects the mission duration,

Fig. 20 shows the same set of “blue triangles” data that was shown in Fig. 17, but with different plot indications. In this figure, the blue and black circles are all simulations from 450 km at solar minimum, and the numbers at each point indicate the particular spacecraft configuration. The results from the MSIS model and the Exponential model have different distributions among the spacecraft configurations, but the MSIS model consistently predicts longer commissioning periods and longer mission lengths. Since this plot keeps all variables constant except for the density model, it elucidates how the different density models lead to different mission lengths.

4.4 Comparison with MinXSS altitude data

Finally, we compare our model predictions with MinXSS altitude data. Since MinXSS re-entered Earth’s atmosphere in May 2017, we can use its altitude data to help validate that the model is making realistic predictions [42, 43]. The starting altitude for MinXSS after deployment was approximately 410 km, and the design of the MinXSS Cube-Sat is most similar to spacecraft configuration 3. Additionally, since MinXSS was deployed from the ISS on May 16, 2016, I pulled another set of data from the MSIS model to match the appropriate deployment dates. The simulation parameters were the following, and the results of this simulation are shown in Fig. 21:

- Starting altitude: 410 km
- Density model: MSIS with starting epoch of May 16, 2016
- Spacecraft configuration: 3

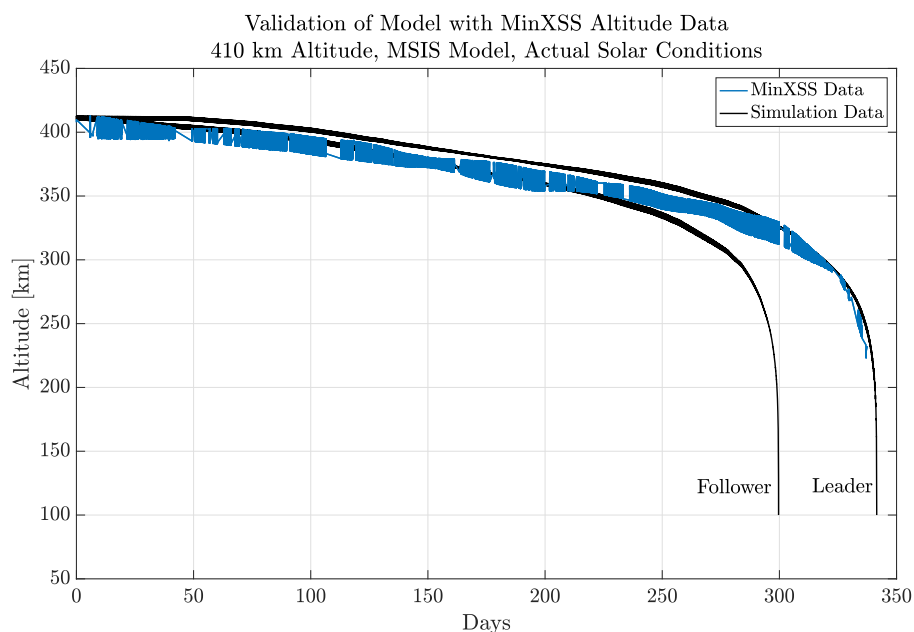


Figure 21: Figure showing a comparison between the actual MinXSS altitude decay and the propagated model using similar initial conditions.

Fig. 21 shows that the actual MinXSS altitude data is in family with the results of the simulation using similar initial conditions. Additional factors that may affect the accuracy of this model as compared with real spacecraft data are discussed in Section 5.

4.5 Adding Additional CubeSats to the Constellation

If two CubeSats can accomplish the mission design, would there be any benefit to adding a third or fourth (or more) spacecraft to the constellation? While this is not a scenario that has been investigated analytically, it is worthy of consideration as a discussion point. Certainly, adding more satellites to the constellation could be advantageous—from an engineering perspective, adding another CubeSat when the mission could be accomplished with two provides margin and redundancy in case of on-orbit failure, though on its own this is likely not sufficient justification for an additional CubeSat. It also provides more

margin on the required in-track separation error; with more satellites, the spacecraft could drift further before a control algorithm would have to be employed to ensure continuous solar observation. From a science perspective, having another spacecraft taking measurements is a fantastic source of verification and calibration (particularly if two of satellites were able to take simultaneous measurements). On-orbit calibration of science instruments can be challenging for low-budget missions, so having another satellite taking simultaneous measurements could be a valuable boon for the project. Although this is typically more important for in-situ measurements, additional spacecraft could provide a stronger spatial component to the data depending on the scientific goal and instrument(s).

Of course, there are also drawbacks to increasing the size of the constellation. More satellites on orbit will require more operational complexity, as well as more time needed on ground assets to downlink data. The cost of the program will also increase due to additional hardware, manufacturing, launch, and operations expenses.

4.6 Asynchronous CubeSat Deployments

One of the initial assumptions of this project is that the two CubeSats are deployed consecutively so that they have essentially the same initial state vector at the start of the propagation. What would happen if one of the deployments were intentionally delayed—would that decrease the time spent in the commissioning phase? To answer this question, we need to consider the speed of deployment. When CubeSats are deployed from the International Space Station, they have a relative ejection speed of 1 to 2 m/s [44], which is only 0.03% of the ISS' orbital speed of 7.67 km/s [45]. While this is certainly possible from a

physics point of view, it may be impractical from an operations standpoint, especially considering the other CubeSat payloads that may be deploying at the same time. Additionally, we would have to ensure that the asynchronous deployment would not occur on either side of an ISS station-keeping maneuver or other change that could affect the initial orbit.

4.7 Results Summary

In this section, I showed that there is a large feasible trade space available for this mission concept. In the baseline simulation, all nine spacecraft configurations produced feasible results, with the shortest mission lasting 575.50 days (1.6 years), and the longest lasting 1306.17 days (3.6 years). In exploring mission duration with the commissioning phase for all simulations, it was clear that higher starting altitudes will produce longer overall mission durations, and that solar minimum conditions provided more favorable durations. In comparing the two density models, we saw that the MSIS model predicts smaller density values at higher altitudes, which naturally leads to configurations that have longer mission durations. Finally, when comparing MinXSS altitude data with a simulation run that had similar starting conditions, we found that simulated altitude decays are within family of the real data, which provides confidence in the model.

5 Applications and Future Work

5.1 Adding a Control Algorithm

Once the two spacecraft have drifted to 180° separation, this mission concept does not currently include a control algorithm to maintain this separation. Since the use of differential drag will necessarily change the altitude of the follower spacecraft, the angle between the two spacecraft's position vectors will continue to change over time, previously shown in Fig. 16. As discussed in Section 2, Planet Labs has developed and released an open-source control algorithm for CubeSat orbit-keeping through differential drag. Considering the success that Planet Labs has achieved with their constellations, it would be advisable to use their algorithm as a baseline and adjust it as needed. This would be the logical next step for this project—currently we can predict what the spacecraft will do naturally, but in order to strengthen the mission profile we would need to include a method for controlling the in-track position.

If this project were to be extended without employing a control algorithm, another exploration could be to determine what portion of the mission has both spacecraft in eclipse. In other words, how much science collection time would be lost if we simply let the spacecraft drift without a control? To first order, we need to look at the geometry between the size of the Earth, the altitude of the orbit, and the direction of incoming sunlight, as shown in Fig.

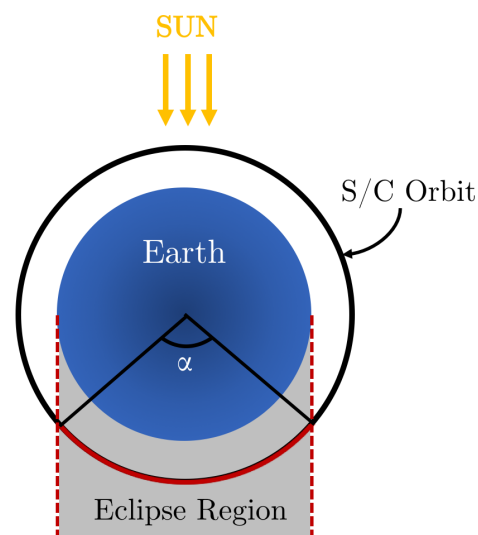


Figure 22: The angle α is directly related to how much of the orbit is spent in eclipse; this value is dependent on the altitude of the orbit as in Eq. 22.

22. The angle α can be found as shown in Eq. 22, and for a 400 km orbit this works out to approximately 136° .

$$\alpha = 180^\circ - 2 \cos^{-1} \left(\frac{R_\oplus}{R_{s/c}} \right) \quad (22)$$

To *guarantee* that one spacecraft will always be in the sun, the angular separation must be between 136° and 224° —this ensures that both spacecraft cannot be in eclipse at the same time. Although this gives a rough estimate, we would also have to consider size of the solar disk as it compares to the atmosphere. In order to observe the Sun effectively, the disk needs to be far enough above the atmosphere to not cause interference. Using this as a starting point, it could be possible to characterize how much science collection time would be lost if the spacecraft were allowed to drift naturally.

5.2 Thermospheric Winds

Another effect that has not been considered in this analysis is the effect on the drag from winds in the thermosphere, which are particularly prevalent at the altitudes under consideration. Thermospheric winds, which are mostly horizontal in nature, originate from variations in atmospheric heating and the diurnal bulge, giving rise to air pressure gradients that induce large-scale motion of particles from the neutral atmosphere [46]. Depending on the direction, these winds can have a direct affect on the drag experienced by a CubeSat, and predicting the strength and direction of these winds is challenging [47]. The calculation described previously in Section 3.3 to calculate the velocity relative to the atmospheric rotation does not include the effect of these winds, only the nominal rotation of the atmosphere

that is caused by the Earth's rotation. In order to incorporate these effects into my simulation, I would need to use empirical data or a model of thermospheric winds to adjust the relative velocity vector that is used in Eq. 18. The Horizontal Wind Model (HWM) is one option—HWM is an empirical model of the neutral winds in the upper thermosphere, which is based on data collected by two satellites and was originally released in 1987. Similar to the MSIS density model, the HWM model takes latitude, longitude, time, and A_p index as inputs, and returns the zonal and meridional winds [48]. Since my model already computes the needed inputs, this model could be a relatively straightforward addition and would likely improve the predictive capability.

5.3 Science Impact of the Commissioning Phase

One point to discuss is that in the proposed concept of operations, the commissioning period would not include science activities. This is a clear disadvantage, as the lifetime of a mission is never guaranteed, and even a small amount of science data is better than none. By restricting science collection to only occur after the spacecraft have drifted to the required angular separation, there is an increased risk of not accomplishing the mission's scientific goals if an early failure were to occur. One idea to reduce this risk is to still have a commissioning period, but only maneuver the spacecraft into their high- or low-drag configurations while they are in eclipse, and maneuver back to solar-pointed after eclipse exit. While there may be an initial period of data loss while the spacecraft are still drifting apart, it would allow science collection to start more immediately after deployment.

5.4 The Effect of Atomic Oxygen

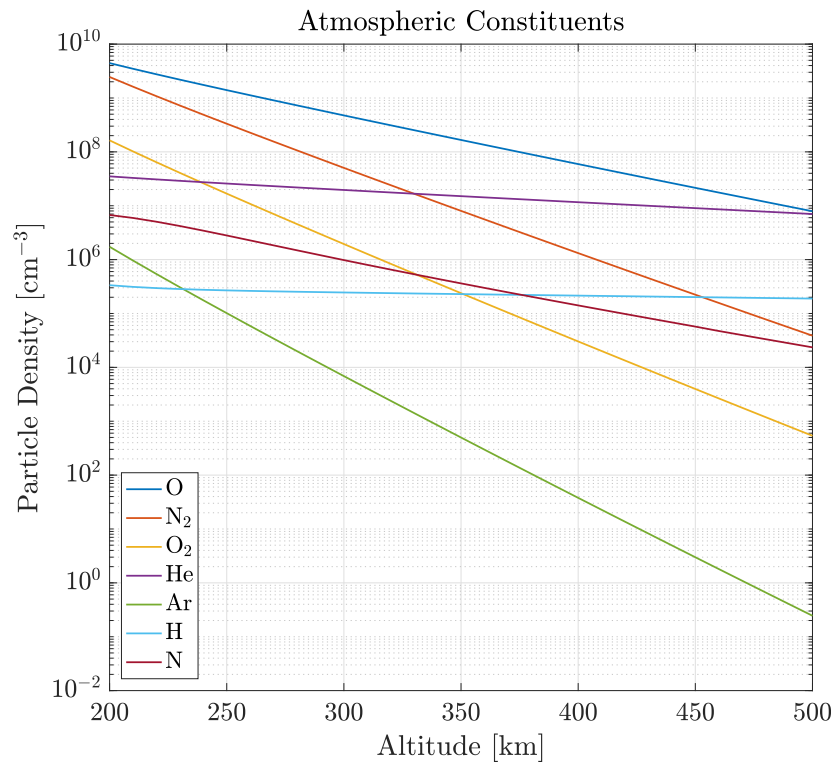


Figure 23: Particle density composition of the atmosphere from 200 to 500 km during mean solar conditions, showing that atomic oxygen is the dominant constituent for the altitudes under consideration in this project [37].

As discussed briefly in Section 3.4, using a C_D of 2.2 is a rough estimate for this value, particularly because of the prevalence of atomic oxygen in the upper atmosphere and its propensity to be adsorbed onto spacecraft surfaces [41]. During mean solar conditions at altitudes between 200 and 500 km, atomic oxygen is the dominant constituent in the atmosphere, as shown in Fig. 23. Since this is the altitude range that I am particularly concerned with, the effect of atomic oxygen could have a significant effect on spacecraft drag. To account for this, a variable value for C_D would need to be incorporated into my model to allow for variation with altitude. In a 2004 study by Kenneth Moe and Mildred M. Moe,

the authors suggested revised values for C_D of 2.24, 2.32, and 2.43, for altitudes of 160, 200, and 250 km respectively. Above 250 km, the behavior of how atomic oxygen is reemitted from a surface changes the estimation of C_D , in particular whether the reemission is diffuse or quasi-specular [41]. The relationship between these behaviors is shown in Fig. 24 for a compact spherical shape and a cylindrical shape with a flat surface in the ram direction.

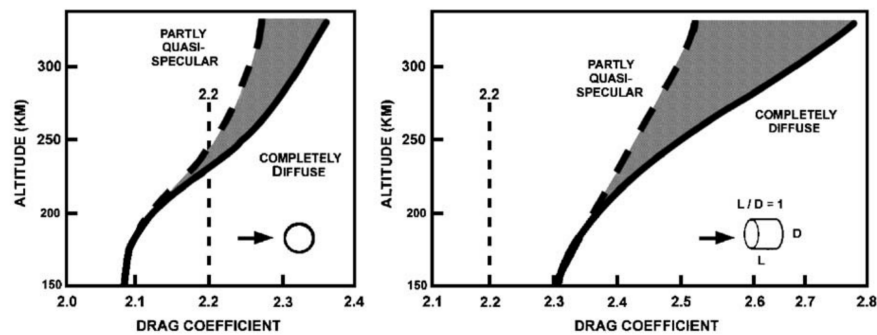


Figure 24: This plot is reproduced from “Gas-surface interactions and satellite drag coefficients” by Moe and Moe, 2004. The authors show that there is a variation in C_D depending on altitude, the shape of the body, and whether the reemission of atomic oxygen is complete diffuse or quasi-specular. This underscores the importance of using a variable value for C_D for a more accurate model.

To highlight how a changing C_D would affect the output, I ran one simulation with variable values of C_D that depend on altitude, while keeping all other parameters the same. The simulation shown in Fig. 25 is for a 450 km starting altitude, at solar minimum, with the MSIS density model for spacecraft configuration 3. As expected, using variable values for C_D reduced the mission duration in this particular case, which follows because larger values of C_D will cause the drag force to be larger, per Eq. 18. The following values were used for C_D :

- Below 160 km, $C_D = 2.24$
- Between 160 km and 200 km, $C_D = 2.32$
- Between 200 km and 250 km, $C_D = 2.43$

- Above 250 km, $C_D = 2.6$ (estimated from Fig. 24)

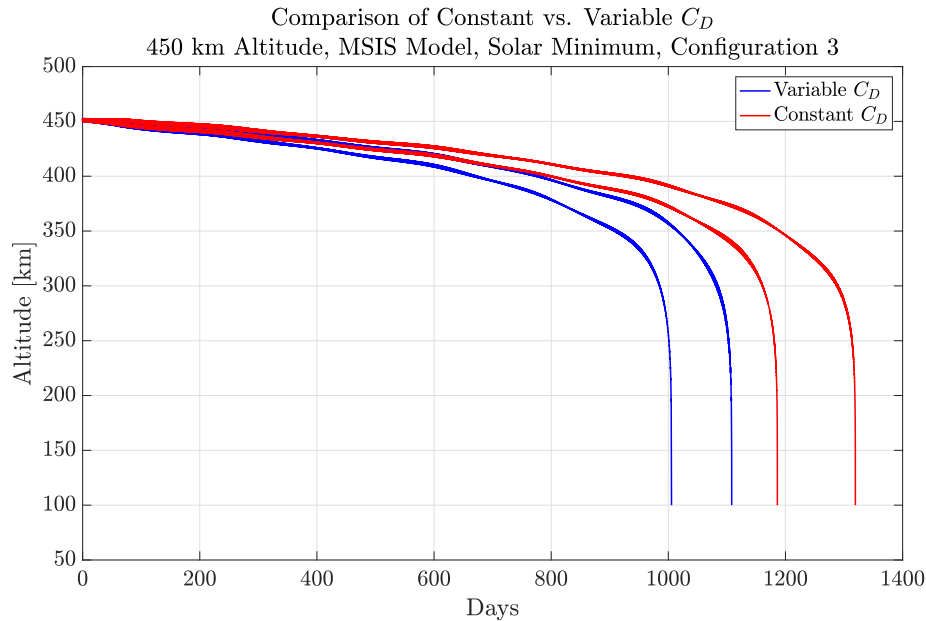


Figure 25: Comparison of the same simulation run with a constant C_D of 2.2 versus a variable C_D as described above. The variable C_D case shows a reduced mission length, which is likely more accurate since the effect of atomic oxygen in the upper atmosphere changes the value of C_D . Note that both cases show the usual leader and follower curves for the two spacecraft.

It is clear from Fig. 25 that using a variable C_D changes the mission length, and based on previous discussion, that this is likely a more accurate depiction of the mission. In future iterations of this work, a variable C_D should be implemented to improve the accuracy.

5.5 A More Comprehensive Gravity Model

Since the Earth is not a perfect sphere, an improvement to this model would incorporate a variable gravity field. There are a variety of gravity models that could be used in place of Newton's law of gravitation, and many involve input parameters that we have computed previously. One recent model is the Earth Gravitational Model 2008 (EGM2008), which is a spherical harmonic model that has coefficients up to degree and order 2159 [49].

EGM2008 uses a combination of Earth-based and satellite data to estimate anomalies in the gravitational field, and is one of many gravity models that can be implemented easily in MATLAB with the function `gravitysphericalharmonic` [50]. This function will take a position vector in Earth-centered Earth-fixed coordinates, which were already computed for the implementation of the NRLMSISE-00 model as discussed in Section 3.3.2, and will output a three-component gravitational acceleration vector for that particular point in space. These values could be implemented in Eq. 8 in place of Newton's law of gravitation to provide a more sophisticated gravity model in future efforts.

5.6 Self-Shadowing of Spacecraft Body by Solar Panels

As discussed in Section 3.4, this model does not account for self-shadowing of the spacecraft body by solar panels, and depending on the spacecraft configuration, this could be a significant effect. In one study of Mars Odyssey and Mars Reconnaissance Orbiter, it was determined that the relevant cross-sectional areas of these two spacecraft can change up to 20% on average if self-shadowing is accounted for, and that the area can also vary within a single orbit depending on atmospheric conditions [51]. Without a detailed analysis it is difficult to estimate the impact that self-shadowing will have on the nine spacecraft configurations, but Fig. 26 shows how the mission duration would be increased if the cross-sectional areas were reduced by 20% while in the solar-pointed configuration (when the same face is always ram-pointed, the area is constant and no self-shadowing occurs).

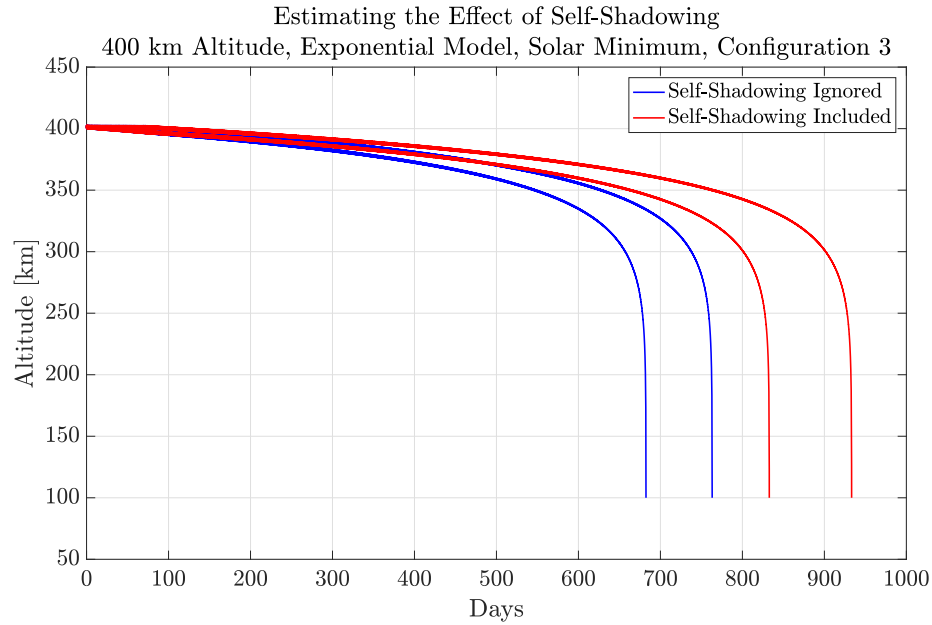


Figure 26: If the cross-sectional areas are reduced by 20% throughout the solar-pointed portion of the mission, the total mission duration increases. This may be a more accurate representation since the current model does not account for self-shadowing. Note that both cases show the usual leader and follower curves for the two spacecraft.

6 Summary

The goal of this work was to explore the feasibility of using a two-CubeSat constellation to achieve continuous solar science from low Earth orbit. By developing a two-body propagator, I was able to run simulations of this concept by varying the inputs for starting altitude, spacecraft configuration, density model, and spacecraft attitude. This resulted in a large trade space of feasible mission designs that could be further reduced with the selection of particular parameters to enable a specific solar science mission. As expected, higher altitudes and solar minimum conditions produce the longest mission durations, and solutions exist for every spacecraft configuration considered. The simulation could be expanded by adding a control algorithm to dynamically control the in-track spacing between in the constellation, which would allow for a more robust concept. Additionally, other physical effects such as thermospheric winds, atomic oxygen adsorption, and self-shadowing could be added to the simulation to enhance the fidelity and accuracy of the model.

References

- [1] Solar Physics Historical Timeline (1223 BC to 250 BC). <https://www2.hao.ucar.edu/Education/solar-physics-historical-timeline-1223-BC-250-BC>. High Altitude Observatory. Accessed: 27 March 2018.
- [2] National Aeronautics and Space Administration. *Our Dynamic Space Environment: Heliophysics Science and Technology Roadmap for 2014-2033*. National Aeronautics and Space Administration, 2014.
- [3] Heliophysics Research. <https://science.nasa.gov/heliophysics/programs/research>. Accessed: 27 March 2018.
- [4] Shanessa Jackson. Upcoming ELaNa CubeSat Launches. <https://www.nasa.gov/content/upcoming-elana-cubesat-launches>, July 2016.
- [5] David A. Vallado. *Fundamentals of Astrodynamics and Applications*. Springer, 2007.
- [6] GOES Space Environment Monitor Data Access. *GOES Space Environment Monitor Data Access*. Accessed: 01 April 2018.
- [7] Delores J. Knipp. *Understanding Space Weather and the Physics Behind It*. McGraw-Hill, 2011.
- [8] Christopher S. Moore, Thomas N. Woods, Amir Caspi, and James P. Mason. The Miniature X-ray Solar Spectrometer (MinXSS) CubeSats: Spectrometer Characterization Techniques, Spectrometer Capabilities, and Solar Science Objectives. *Space Telescopes and Instrumentation 2016: Ultraviolet to Gamma Ray*, November 2016.
- [9] Rob Garner. Space Station-Bound CubeSat to Study Sun's X-Rays. <https://www.nasa.gov/feature/goddard/minxss-cubesat-launches-to-iss-to-study-sun-s-soft-x-rays>, December 2015. Accessed: 18 April 2018.
- [10] Christopher S. Moore, Thomas N. Woods, Amir Caspi, and James P. Mason. The Miniature X-ray Solar Spectrometer (MinXSS) CubeSats: spectrometer characterization techniques, spectrometer capabilities, and solar science objectives. *Space Telescopes and Instrumentation 2016: Ultraviolet to Gamma Ray*, November 2016.
- [11] X. Li, Q. Schiller, L. Blum, S. Califf, H. Zhao, W. Tu, D. L. Turner, D. Gerhardt, S. Palo, and et al. Kanekal, S. First results from CSSWE CubeSat: Characteristics of relativistic electrons in the near-Earth environment during the October 2012 magnetic storms. *Journal of Geophysical Research: Space Physics*, 118(10):64896499, 2013.
- [12] A. W. Breneman, A. Crew, J. Sample, D. Klumpar, A. Johnson, O. Agapitov, M. Shumko, D. L. Turner, O. Santolik, and et al. Wygant, J. R. Observations Directly Linking Relativistic Electron Microbursts to Whistler Mode Chorus: Van Allen Probes and FIREBIRD II. *Geophysical Research Letters*, 44(22), 2017.
- [13] Lori J. Keesey. NASA begins checkout of Dellinger spacecraft designed to improve robustness of CubeSat platforms. *GSFC News*, December 2017.

- [14] Xinlin Li, Richard Selesnick, Quintin Schiller, Kun Zhang, Hong Zhao, Daniel N. Baker, and Michael A. Temerin. Measurement of electrons from albedo neutron decay and neutron density in near-earth space. *Nature*, 552(7685):382385, 2017.
- [15] Grant Bonin, Niels Roth, Scott Armitage, Josh Newman, Ben Risi, and Robert E. Zee. Canx-4 and canx-5 precision formation flight: Mission accomplished! *29th Annual AIAA/USU Conference on Small Satellites*, August 2015.
- [16] Sreeja Nag, Joseph L. Rios, David Gerhardt, and Camvu Pham. CubeSat constellation design for air traffic monitoring. *Acta Astronautica*, 128:180193, 2016.
- [17] Steven C. Reising, Todd C. Gaier, Christian D. Kummerow, V. Chandrasekar, Shannon T. Brown, Sharmila Padmanabhan, Boon H. Lim, Susan C. Van Den Heever, Tristan S. L'Ecuyer, and et al. Ruf, Christopher S. Overview of Temporal Experiment for Storms and Tropical Systems (TEMPEST) CubeSat Constellation Mission. *2015 IEEE MTT-S International Microwave Symposium*, 2015.
- [18] C. S. Fish, C. M. Swenson, G. Crowley, A. Barjatya, T. Neilsen, J. Gunther, I. Azeem, M. Pilinski, R. Wilder, and et al. Allen, D. Design, Development, Implementation, and On-orbit Performance of the Dynamic Ionosphere CubeSat Experiment Mission. *Space Science Reviews*, 181(1-4):61120, June 2014.
- [19] Joseph Gangestad, Darren Rowen, Brian Hardy, Christopher Coffman, and Paul O'Brien. *CubeSat Developers' Workshop*. 2015.
- [20] Cyrus Foster, Henry Hallam, and James Mason. Orbit Determination and Differential-Drag Control of Planet Labs Cubesat Constellations. *American Astronautical Society, AIAA Astrodynamics Specialist Conference*, September 2015.
- [21] Cyrus Foster, James Mason, Vivek Vittaldev, Lawrence Leung, Vincent Beukelaers, Leon Stepan, and Rob Zimmerman. Constellation Phasing with Differential Drag on Planet Labs Satellites. *Journal of Spacecraft and Rockets*, 55(2):473483, 2018.
- [22] Mary Morris and Christopher S. Ruf. Determining Tropical Cyclone Surface Wind Speed Structure and Intensity with the CYGNSS Satellite Constellation. *Journal of Applied Meteorology and Climatology*, 56(7):18471865, 2017.
- [23] Karen Fox. Seeing Earth's Magnetism. <https://nasaviz.gsfc.nasa.gov/12280>, June 2016. Accessed: 18 April 2018.
- [24] C. P. Escoubet, M. Fehringer, and M. Goldstein. The Cluster Mission. *Annales Geophysicae*, 19(10/12):11971200, 2001.
- [25] European Space Agency. Swarm—The Earth's Magnetic Field and Environment Explorers. *Reports For Mission Selection: The Six Candidate Earth Explorer Missions*, April 2004.
- [26] C. R. Tooley, R. K. Black, B. P. Robertson, J. M. Stone, S. E. Pope, and G. T. Davis. The Magnetospheric Multiscale Constellation. *Magnetospheric Multiscale*, 199(1-4):2376, March 2016.
- [27] Tristan S. L'Ecuyer and Jonathan H. Jiang. Touring the atmosphere aboard the A-Train. *Physics Today*, 63(7):3641, 2010.

- [28] Tony Greicius. CloudSat Exits the “A-Train”.
<https://www.nasa.gov/feature/jpl/cloudsat-exits-the-a-train>, February 2018.
 Accessed: 01 April 2018.
- [29] MinXSS: Now in Science Mode!
<http://lasp.colorado.edu/home/minxss/2016/05/28/minxss-now-in-science-mode/>,
 May 2016. Accessed: 18 April 2018.
- [30] T. S. Kelso. NORAD Two-Line Element Sets - Current Data.
<https://celestrak.com/NORAD/elements/>, April 2018. Accessed: 02 April 2018.
- [31] External Cygnus Deployment.
<http://nanoracks.com/products/external-cygnus-deployment/>. Accessed: 02 April 2018.
- [32] Solar radio flux—Archive of measurements.
<http://www.spaceweather.gc.ca/solarflux/sx-5-en.php>. Accessed: 05 April 2018.
- [33] Howard D. Curtis. *Orbital Mechanics for Engineering Students*. Elsevier, 2014.
- [34] John Kennewell. Satellite Orbital Decay Calculations. *Australian Space Weather Agency*, page 111, 1999.
- [35] Mike Lockwood, Mathew J. Owens, Luke A. Barnard, Chris J. Scott, Clare E. Watt, and Sarah Bentley. Space climate and space weather over the past 400 years: 2. Proxy indicators of geomagnetic storm and substorm occurrence. *Journal of Space Weather and Space Climate*, January 2018.
- [36] Yiding Chen, Libo Liu, and Weixing Wan. Does the F10.7index correctly describe solar EUV flux during the deep solar minimum of 2007-2009? *Journal of Geophysical Research: Space Physics*, 116(A04304), April 2011.
- [37] NRLMSISE-00 Atmosphere Model. *Community Coordinated Modeling Center, Goddard Space Flight Center*. <https://ccmc.gsfc.nasa.gov/modelweb/models/nrlmsise00.php>.
- [38] K. Labitzke, J. J. Barnett, and B. Edwards. *Middle Atmosphere Program, Volume 16: Atmospheric Structure and Its Variation in the Region 20 to 120 Km. Draft of a New Reference Middle Atmosphere*. ICSU Scientific Committee on Solar Terrestrial Physics, 1985.
- [39] A. E. Hedin. MSISE Model.
<https://ccmc.gsfc.nasa.gov/models/modelinfo.php?model=MSISE>.
- [40] atmosnrlmsise00. <https://www.mathworks.com/help/aerotbx/ug/atmosnrlmsise00.html>.
 Accessed: 05 April 2018.
- [41] Kenneth Moe and Mildred M. Moe. Gassurface interactions and satellite drag coefficients. *Planetary and Space Science*, 53(8):793801, 2005.
- [42] The Miniature X-ray Solar Spectrometer (MinXSS).
<http://lasp.colorado.edu/home/minxss/>. Accessed: 19 April 2018.

- [43] The MinXSS CubeSat: Level 0D Science Data Description. <http://lasp.colorado.edu/home/minxss/data/level-0d/>. Accessed: 19 April 2018.
- [44] NanoRacks CubeSat Deployer. https://www.nasa.gov/mission_pages/station/research/experiments/1350.html, March 2018. Accessed: 19 April 2018.
- [45] Dirk Matussek. Current Position of the ISS. <http://iss.astroviewer.net/>, April 2018. Accessed: 19 April 2018.
- [46] H. Rishbeth. Thermospheric winds and the F-region: A review. *Journal of Atmospheric and Terrestrial Physics*, 34(1):147, 1972.
- [47] David Mostaza Prieto, Benjamin P. Graziano, and Peter C.E. Roberts. Spacecraft drag modelling. *Progress in Aerospace Sciences*, 64:5665, 2014.
- [48] A. E. Hedin. Horizontal wind model (HWM) (1990). *Planetary and Space Science*, 40(4):556557, 1992.
- [49] Nikolaos K. Pavlis, Simon A. Holmes, Steve C. Kenyon, and John K. Factor. The development and evaluation of the Earth Gravitational Model 2008 (EGM2008). *Journal of Geophysical Research: Solid Earth*, 117(B4), 2012.
- [50] gravitysphericalharmonic. <https://www.mathworks.com/help/aerotbx/ug/gravitysphericalharmonic.html>. Accessed: 23 April 2018.
- [51] Erwan Mazarico, Maria T. Zuber, Frank G. Lemoine, and David E. Smith. Effects of Self-Shadowing on Nonconservative Force Modeling for Mars-Orbiting Spacecraft. *Journal of Spacecraft and Rockets*, 46(3):662669, 2009.
- [52] Rein Ise and Eugene H. Cagle. The Apollo telescope mount on Skylab. *Acta Astronautica*, 1(11-12):13151329, 1974.
- [53] John Wilkinson. *Probing the Sun*. Springer, 2012.
- [54] Solwind instrument destroyed in test. *Eos, Transactions American Geophysical Union*, 66(44):739, 1985.
- [55] K. T. Strong and J. T. Schmelz. The Solar Maximum Mission. *The Many Faces of the Sun*, page 118, 1999.
- [56] Y. Tanaka. Introduction to HINOTORI. *Solar Physics*, 86(1-2):36, July 1983.
- [57] Y. Ogawara, T. Takano, T. Kato, T. Kosugi, S. Tsuneta, T. Watanabe, I. Kondo, and Y. Uchida. The Solar-A Mission: An Overview. *Solar Physics*, 136(1):116, 1991.
- [58] Solar and Heliospheric Observatory. <https://sohowww.nascom.nasa.gov/>. Accessed: 30 March 2018.
- [59] J. L. Kohl, L. D. Gardner, L. Strachan, R. Fisher, and M. Guhathakurta. Spartan 201 coronal spectroscopy during the polar passes of Ulysses. *Space Science Reviews*, 72(1-2):2938, 1995.

- [60] S. M. Bailey, T. N. Woods, C. A. Barth, S. C. Solomon, L. R. Canfield, and R. Korde. Measurements of the solar soft X-ray irradiance by the Student Nitric Oxide Explorer: First analysis and underflight calibrations. *Journal of Geophysical Research: Space Physics*, 105(A12):2717927193, January 2000.
- [61] I. J. Burt. Transition Region and Coronal Explorer Mission. *1996 IEEE Aerospace Applications Conference. Proceedings.*, August 2002.
- [62] Sun sets for a NASA solar monitoring spacecraft. <https://www.jpl.nasa.gov/news/news.php?feature=4252>, August 2014. Accessed: 23 April 2018.
- [63] S. M. Hill, V. J. Pizzo, C. C. Balch, D. A. Biesecker, P. Bornmann, E. Hildner, L. D. Lewis, R. N. Grubb, M. P. Husler, K. Prendergast, and et al. The NOAA Goes-12 Solar X-Ray Imager (SXI) 1. Instrument, Operations, and Data. *Solar Physics*, 226(2):255281, 2005.
- [64] G. J. Hurford, E. J. Schmahl, R. A. Schwartz, A. J. Conway, M. J. Aschwanden, A. Csillaghy, B. R. Dennis, C. Johns-Krull, S. Krucker, R. P. Lin, and et al. The RHESSI Imaging Concept. *The Reuven Ramaty High-Energy Solar Spectroscopic Imager (RHESSI)*, page 6186, 2003.
- [65] W. Marchant, M. Hurwitz, M. Sholl, and E.R. Taylor. Status of CHIPS: A NASA University Explorer astronomy mission. *Proceedings, IEEE Aerospace Conference*.
- [66] Gary Rottman. The SORCE Mission. *The Solar Radiation and Climate Experiment (SORCE)*, page 725.
- [67] Takashi Sakurai. The Hinode Mission. *Solar Physics*, 243(1), 2007.
- [68] M. L. Kaiser, T. A. Kucera, J. M. Davila, O. C. St. Cyr, M. Guhathakurta, and E. Christian. The STEREO Mission: An Introduction. *The STEREO Mission*, page 516, 2008.
- [69] G. Schmidtke, C. Frhlich, and G. Thuillier. ISS-SOLAR: Total (TSI) and spectral (SSI) irradiance measurements. *Advances in Space Research*, 37(2):255264, 2006.
- [70] A. S. Ulyanov, S. A. Bogachev, and S. V. Kuzin. Bright points and ejections observed on the sun by the KORONAS-FOTON instrument TESIS. *Astronomy Reports*, 54(10):948957, 2010.
- [71] Solar Dynamics Observatory. <https://sdo.gsfc.nasa.gov/>. Accessed: 30 March 2018.
- [72] Costantino Sigismondi. The Picard Satellite Mission For Solar Astrometry. *International Journal of Modern Physics: Conference Series*, 12:400404, 2012.
- [73] B. De Pontieu, A. M. Title, J. R. Lemen, G. D. Kushner, D. J. Akin, B. Allard, T. Berger, P. Boerner, M. Cheung, C. Chou, and et al. The Interface Region Imaging Spectrograph (IRIS). *Solar Physics*, 289(7):27332779, 2014.
- [74] Joe Burt and B. Smith. Deep Space Climate Observatory: The DSCOVR mission. *2012 IEEE Aerospace Conference*, 2012.
- [75] Candace Carlisle, Ronnice Wedge, Dong Wu, Harry Stello, and Renee Robinson. *Total and Spectral Solar Irradiance Sensor (TSIS) Project Overview*. 2015.

- [76] N. J. Fox, M. C. Velli, S. D. Bale, R. Decker, A. Driesman, R. A. Howard, J. C. Kasper, J. Kinnison, M. Kusterer, D. Lario, and et al. The Solar Probe Plus Mission: Humanity's First Visit to Our Star. *Space Science Reviews*, 204(1-4):748, November 2015.
- [77] D. Mueller, R. G. Marsden, O. C. St. Cyr, and H. R. Gilbert. Solar Orbiter. *Solar Physics*, 285(1-2):2570, 2012.
- [78] S. Seetha and S. Megala. Aditya-L1 Mission. *Current Science*, 113(04):610, 2017.

Appendix

Table 9: Summary of space-based missions for remote sensing measurements of the Sun, sorted by launch year.

Mission	Scientific Goals	Year
Apollo Telescope Mount [52]	First manned solar observatory in space. Studied rapid large-scale movement in corona, flare trigger mechanisms and energy relationships, relationships between coronal holes and the solar wind, and bright spots in the X-ray corona	1973
Helios-A and Helios-B [53]	Suite of 11 instruments, 9 of which take in-situ and remote sensing measurements of solar phenomena and solar processes	1974, 1976
Solwind [54]	Study of the sun's corona at a height of 3-10 solar radii. Held record for longest continuous observation of corona when it was destroyed in an anti-satellite missile test by the U.S. military.	1979
SolarMax/SMM [55]	Investigate the origins and processes that result in solar flares	1980
Hinotori (Astro-A) [56]	Imaging of solar flares in the X-ray spectrum, from 10 keV to 40 keV, and spectroscopy with a Bragg spectrometer to study X-ray emission lines from 1.7 to 2.0 Å	1981
Yohkoh (Solar-A) [57]	Study solar flares, particularly high-energy phenomena in the X-ray and gamma-ray spectra	1991
Solar and Heliospheric Observatory (SOHO) [58]	Suite of 12 instruments designed to study the Sun from the core to the corona	1995
SPARTAN-201 [59]	Investigation of the interaction between the sun and outflowing charged particles	1997
Student Nitric Oxide Explorer (SNOE) [60]	Daily observations of solar soft X-ray irradiance via five-channel solar X-ray photometer	1998
TRACE [61]	Exploration of the dynamics and evolution of the solar atmosphere from photosphere to corona.	1998
AcrimSat [62]	Measurement of total solar irradiance (TSI) via cavity optometrics	1999
Solar X-Ray Imager (SXI) [63]	On GOES 12-15, continuous full-disk soft X-ray solar imagery.	2001

Mission	Scientific Goals	Year
RHESSI [64]	Measurement of solar hard X-rays between 3 keV and 17 MeV via rotating modulation collimators.	2002
CHIPS [65]	Extreme ultraviolet (EUV) and in situ particle experiment exploring the interstellar medium. Converted to EUV imaging of the sun from 2006-2008.	2003
SORCE [66]	Measurement of solar irradiance incident on Earth's atmosphere; includes instrument for TSI as well as specific band passe.	2003
Hinode (Solar-B) [67]	Investigation of energy transfer from photosphere to upper solar atmosphere. Successor to Yohkoh (Solar-A) mission.	2006
Stereo-A and Stereo-B [68]	Understanding the initiation and propagation mechanisms of coronal mass ejections via simultaneous observations from two heliocentric spacecraft a great distance apart.	2006
ISS-SOLAR [69]	Measurement of total solar irradiance and spectral solar irradiance	2008
Koronas-Foton [70]	X-ray and UV solar imager. Failed roughly 8 months after launch.	2009
Solar Dynamics Observatory (SDO) [71]	Image the solar corona in multiple wavelengths simultaneously, study oscillations and the magnetic field at the photosphere, measure solar extreme-ultraviolet (EUV) irradiance and monitor its variations	2010
Picard [72]	Milliarcsecond measurement of solar radius and evaluation of W, the logarithmic ratio of radius and luminosity.	2010
IRIS [73]	Recording simultaneous spectra and images of the photosphere, chromosphere, transition region, and corona of the sun. UV instrument sensitive to plasma emissions at temperatures between 5000 K and 10 MK	2013
DSCOVR [74]	Monitoring of solar weather, primarily providing rapid warning for solar flares and other extreme solar events.	2015
MinXSS [8]	First solar science CubeSat. Measured soft X-ray (SXR) flux in effort to understand its effect on Earth's ionosphere and thermosphere.	2015
TSIS [75]	Measure total and spectral irradiance of the Sun for five years from the ISS platform	2017
Parker Solar Probe [76]	In-situ measurements of low solar corona. Goals include determination of structure and dynamics of coronal magnetic field, study of solar corona and wind heading and acceleration, and acceleration of solar energetic particles.	2018

Mission	Scientific Goals	Year
Solar Orbiter [77]	Investigation of creation and control mechanisms of the heliosphere using a suite of instruments including in-situ particle detection and remote sensing at many wavelengths.	2019
Aditya-L1 [78]	Study of the sun's photosphere in UV and hard X-ray, chromosphere in UV, and corona in visible and near infrared from the Sun-Earth L1 point	2019, 2020